

Trapping and Beamloading in hybrid Plasma Wakefield Accelerator schemes

Alexander Knetsch

January 3, 2017

CONTENTS

1. theory	4
1.1 Electromagnetism	4
1.2 Plasma physics	4
1.2.1 electromagnetic waves in plasmas	6
1.2.2 Underdense ionization with ultrashort laser pulses	7
1.3 PWFA theory	9
1.4 The linear regime	9
1.5 The blowout regime	10
1.6 Descriptions for the blowout regime	10
1.7 Physics of particle acceleration	11
1.7.1 Single electron dynamics	11
1.7.2 Liouville Theorem	12
1.7.3 Courant-Snyder coefficients, brightness and emittance	12
1.7.4 $\alpha\beta\gamma$	14
1.8 Electron Trapping in plasma accelerators	14
1.8.1 Trapping position and bunch compression	16
1.9 Acceleration methods in PWFA	18
1.9.1 External injection - Double bunch	19
1.9.2 Density Downramp injection	20
1.9.3 Plasma Torch	21
1.9.4 ionization injection	22
1.9.5 Trojan Horse injection	23
1.10 Trapping behaviour for the Trojan Horse Injection	23
1.10.1 The role of the ionization front	23
1.10.2 Dark current mitigation	24
1.10.3 Downramp assisted Trojan Horse	24
1.11 numerical modeling of Trojan Horse injection	24
1.11.1 emittance growth from space charge	24
1.11.2 Laser parameter variations	24
2. experiment	28
2.1 The FACET experimental setup	28
2.1.1 LINAC	28
2.1.2 The FACET laser system	28
2.1.3 E210 setup	28
2.1.4 Imaging spectrometer	28
2.1.5 Laser energy calibration	28

2.2	Electro Optical Sampling (EOS)	32
2.3	Ionization test	35
2.4	Plasma glow diagnostic	35
2.5	Charge calibration	37
2.6	Result: Plasma Torch injection	39
2.7	Result: Trojan Horse injection	39

1. THEORY

1.1 Electromagnetism

$$\vec{\nabla} \cdot \vec{E} = \frac{\rho}{\epsilon_0} \quad (1.1)$$

$$\vec{\nabla} \cdot \vec{B} = 0 \quad (1.2)$$

$$\vec{\nabla} \times \vec{E} = -\frac{\partial \vec{B}}{\partial t} \quad (1.3)$$

$$\vec{\nabla} \times \vec{B} = \mu_0 \vec{j} + \mu_0 \epsilon_0 \frac{\partial \vec{E}}{\partial t}. \quad (1.4)$$

\vec{E} and \vec{B} are the electric and magnetic field and \vec{j} and ρ is the current density and charge density. ϵ_0 and μ_0 are the vacuum dielectric constant and the vacuum permeability. They are connected with the vacuum speed of light c through the relation $c = 1/\sqrt{\mu_0 \epsilon_0}$

$$\vec{F} = \frac{d\vec{p}}{dt} = q(\vec{E} + \frac{\vec{v}}{c} \times \vec{B}) \quad (1.5)$$

1.2 Plasma physics

There are several definitions of a plasma, but one of the most appealing one that we will follow in this work can be found in the classic textbook by Francis F. Chen: "A plasma is a quasineutral gas of charged and neutral particles which exhibits collective behavior" [1]. Regarding the gas types we will conveniently assume them to be electrons, ions and neutral atoms and comment that other particles as well can fit the definition of a plasma, but such exotic compositions are beyond the scope of this work. As plasmas are electromagnetically interacting a common and very useful way to describe it on a fundamental level is with the help of the Maxwell equation.

In a fluid description it makes also sense to assume that no particles are created or destroyed which is the origin of the continuity equation

$$\frac{\partial \rho}{\partial t} + \vec{\nabla} \cdot (\rho \vec{v}) = 0. \quad (1.6)$$

Plasma frequency

Electrons and ions in a plasma can be described as two fluids, each following the fluid dynamics and interacting via electrodynamics and collisions.

A displacement of the electron fluid with respect to the ion fluid leads to strong electric fields, acting upon both as a restoring force, but as $m_i \gg m_e$, the electron response is much quicker

which is why these kind of plasma oscillations are dominated by the electrons, while the ions can be considered inert.

Starting from equation (1.13) with the relation of the electric field and its potential being $\vec{E} = -\nabla\Phi$

$$\epsilon_0 \nabla \vec{E} = q_e(n_i - n_e) \quad (1.7)$$

becomes for small perturbations $n' = n_e + \delta n$

$$\epsilon_0 \nabla \vec{E} = q_e \delta n). \quad (1.8)$$

The solution to this differential equation is a harmonic density oscillation

$$n(x, t) = \delta n \exp(i(kx - \omega_p t)). \quad (1.9)$$

The characteristic frequency of this oscillation

$$\omega_p = \sqrt{\frac{n_e q_e^2}{\epsilon_0 m_e}} \quad (1.10)$$

is called the *Plasma frequency* and is one of the most important parameters in plasma physics. In the context of plasma accelerators it is convenient to also consider the wavelength associated with the plasma oscillations, the *Plasma wavelength*

$$\lambda_p = 2\pi \frac{\omega_p}{c}. \quad (1.11)$$

The plasma wavelength gives the rough longitudinal length of a plasma wake. Typical values for example for a plasma density $n_e = 1 \times 10^{17} \text{ cm}^{-3}$ are

$$\begin{aligned} \omega_p &\approx 56400 \sqrt{n_e [\text{cm}^{-3}]} \approx 1.8 \times 10^{18} \text{ 1/s} \\ \lambda_p &\approx 105.6 / \sqrt{n_e [10^{17} \text{ cm}^{-3}]} [\mu\text{m}] = 105.6 \text{ } \mu\text{m}. \end{aligned}$$

Debye Shielding

The concept of *quasi-neutrality* roots in the shielding behavior of the ions and electrons of charges inside the plasma. A positive net charge e.g. originating from a difference in ion density n_i and electron density n_e at a temperature T would attract electrons and lead to an electron distribution

$$f(u) \propto \exp(-\frac{1}{2} m_e v^2 + q_e/(k_B T)). \quad (1.12)$$

With the Poisson Equation

$$\epsilon_0 \frac{d^2 \Phi}{dx^2} = -q_e(n_e - n_i) \quad (1.13)$$

$$= q_e n_e (\exp(q_e \Phi / (k_B T)) - 1) \quad (1.14)$$

$$\approx q_e n_e (q_e \Phi / (k_B T) + \dots) \quad (1.15)$$

we can now derive the potential in the plasma

$$\Phi = \Phi_0 \exp(-|x|/\lambda_D) \quad (1.16)$$

with the information about the range of the shielded Coulomb field embedded in the Debye Radius

$$\lambda_D = \sqrt{\frac{\epsilon_0 k_B T}{n_e q_e^2}}. \quad (1.17)$$

We can see that a plasma with an edge length $L \gg \lambda_D$ would have its Coulomb fields shielded and appear to an outside observer to be charge-neutral.

1.2.1 electromagnetic waves in plasmas

It is worth noting that the Debye Shielding assumes a thermalized plasma and is not the right idea of a plasma reaction to a rapid change in charge on a femtosecond timescale. The more appropriate figure of merit is to look directly at the propagation of electromagnetic waves in plasma which we will deduct now following [2].

The electromagnetic wave propagation needs to be calculated by applying the Maxwell equations 1.1 so that one gets the differenctial equation.

$$\vec{\nabla} \times \vec{\nabla} \times \vec{E} + c^{-2} \frac{\partial^2 \vec{E}}{\partial t^2} = -\frac{1}{\epsilon_0 c^2} \frac{\partial \vec{j}}{\partial t} \quad (1.18)$$

In plasma the current density is not 0, but only electronic flow velocity \vec{v}_e needs to be taken into account for the high frequencies we are considering in this work so that

$$\vec{j} = -q_e n_e \vec{v}_e \quad (1.19)$$

Equation (1.18) can be solved with an exponential Ansatz for a linear wave

$$\vec{E} = E_0 e^{(ikx-i\omega t)} \quad (1.20)$$

so that equation (1.18) becomes

$$\nabla \times \nabla \times \vec{E} - k^2 \eta^2 \vec{E} = \frac{v_g v_{ph}}{c^2} \quad (1.21)$$

with an index of refraction in an absorption-free plasma

$$\eta = \sqrt{1 - \frac{\omega_p^2}{\omega^2}}. \quad (1.22)$$

Equation (1.22) can be interpreted as a criterion for the propagation. For $\omega_p > \omega$ η becomes imaginary which is physically equivalent to a reflection of the wave.

The measure of the depth of intrusion is the skin depth

$$k_p^{-1} = \frac{c}{\sqrt{\omega_p^2 - \omega^2}} \stackrel{\omega_p \gg \omega}{=} \frac{c}{\omega_p} \quad (1.23)$$

Ergo for the reflection to transparency transitions i.e. at $\omega_p = \omega$ a so called critical plasma density

$$n_e^{\text{crit.}} = \frac{\epsilon_0 m_e \omega^2}{q_e^2} \quad (1.24)$$

can be defined.

In this work the propagation of several fs short laser pulses with a central wavelength of $\lambda = 800$ nm are going to be looked at. The reason is that experimentally these are the typical parameters for a Titan-Saphire (Ti:Sa) laser system which is the most common one.

For such a laser system the critical density in equation (1.24) is $n_{\text{crit.}} = 1.7 \times 10^{21} \text{ cm}^{-3}$. As the electron densities essential to the scope of this work are not going to exceed $1 \times 10^{19} \text{ cm}^{-3}$, we can for the context of this work safely assume that the plasma is opaque for laser light. Such a plasma is also called *underdense* with respect to the laser frequency.

1.2.2 Underdense ionization with ultrashort laser pulses

Subpicosecond laser pulses when sufficiently intense, can be used to easily ionize a gas to a plasma. The description of the underlying physics can be divided into three different regimes, the single-or multiphoton ionization (MPI), the tunnel ionization (TI) and the Barrier suppression ionization (BSI). Multiphoton ionization describes the absorption of one or several photons simultaneously by a bound electron such that the combined energy $\sum \hbar\omega_{\text{Laser}}$ exceeds the electron's potential energy and it is released into continuum. In that sense MPI is necessarily an alternating current (AC) effect, as several laser oscillations need to act upon the electron. TI and BSI on the other hand describe an ionization that occurs due to the deformation of the ion potential, which means that the electron is ionized on a time scale on which the laser field can be assumed to be constant, i.e. a DC effect. A handy parameter to distinguish between the regime of multi-photon and tunneling ionization is the Keldysh parameter

$$\gamma_K = \sqrt{\frac{\xi_{\text{ion}}}{2U_p}}, \quad (1.25)$$

A measure of the amount of laser oscillations the electron endures until its ionization that compares the binding energy ξ_{ion} of an electron in an atomic potential to the ponderomotive energy $U_p = \frac{q_e^2 E^2}{4m_e \omega_L}$ carried out by the laser pulse.

For a Keldysh parameter $\gamma_K < 1$ tunnelling ionization is the dominating effect and for $\gamma_K > 1$ MPI prevails.

In this work we will work with laser intensities up to $1 \times 10^{16} \text{ W/cm}^{-2}$ at a wavelength of $\lambda_{\text{Las}} = 800$ nm which corresponds to a $\gamma_K < 1$ regime.

Tunneling Ionization can be well described with the Ammosov-Delone-Krainov (ADK) model.

In [3] the authors have extended the tunnel ionization probability of electrons in a hydrogen atom to arbitrary atoms. For example for atoms with orbital quantum number $n* \gg 1$ and l and its projection m the tunneling ionization probability for an electron at a binding energy ξ_{ion} being excited by a laser with peak electric field E is

$$w = C_{n*l*}^2 \left(\frac{3E}{\pi E_0} \right) \xi_{\text{ion}} \frac{(2l+1)(l+|m|)!}{2^{|m|}|m|!(l-|m|)!} \left(\frac{2E_0}{E} \right)^{2n*-|m|-1}. \quad (1.26)$$

$n* = Z/\sqrt{2E}$ with the ionization level Z and $E_0 = \sqrt{2E}$. $C_{n*l*} = (\frac{2q_e}{n*})^{n*}/\sqrt{2\pi n*}$.

In [4] Bruhwiler et al. have developed an approximated equation which is optimized for its application in numerical operations such as PIC codes, where the ADK ionization rate is

$$W_{\text{ADK}} = 1.52 \times 10^{15} \frac{4n_{\text{eff}}^* \xi_{\text{ion}} [\text{eV}]}{n_{\text{eff}}^* \Gamma(2n_{\text{eff}}^*)} \left(20.5 \frac{\xi_{\text{ion}}^{3/2} [\text{eV}]}{E [\text{GV/m}]} \right)^{2n_{\text{eff}}^*-1} \times \exp(-6.83 \frac{\xi_{\text{ion}}^{3/2} [\text{eV}]}{E [\text{GV/m}]}) \quad (1.27)$$

for an element to the ionization level Z with its ionization energy ξ_{ion} . $n_{\text{eff}}^* \approx 3.69Z/\xi_{\text{ion}}$ is the effective principal quantum number. A list of ionization energies can be found in [5].

ionization gap

Since the ionization rates increase rapidly with electric field, the difference between no ionization and full ionization of a certain ionization level is determined by only slight changes in electric field strength. Plasma density profiles from short laser pulse ionization can therefore be controlled via the laser pulse intensity distribution or just its total energy. Furthermore, intelligent mixing of gases with different ionization energies can allow for distinct ionization of a low ionization threshold (LIT) component into plasma while the other high ionization threshold (HIT) component remains gaseous.

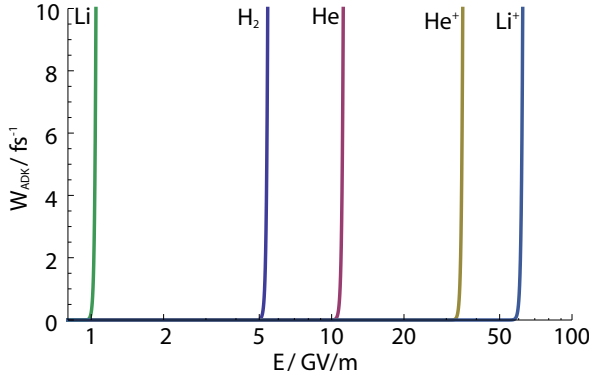


Fig. 1.1: Tunnel ionization rate versus electric field strength in a log-lin plot.

Graph (1.1) depicts the ionization rate over the electric field in a logarithmic plot. The ionization rates of Lithium and Helium qualify well as HIT and LIT composition with a large gap in ionization rates, but lithium with its vaporizing temperature of 1603 K [6] requires external heating to become gaseous, which adds complexity to an experimental setup. A good alternative that does not require any heating is the combination of hydrogen and helium which is used extensively in the context of this work.

Plasma density profiles from laser ionization

The actual ionization ratio of a gas with plasma density at a given point in space in the lab frame for full ionization n_0 is then obtained by integrating

$$\frac{n_e(t)}{n_0} = 1 - \exp\left(-\int_{-\infty}^t W_{ADK}(t')dt'\right). \quad (1.28)$$

As we treat ultrashort pulses, the time scales in which the ionization occurs is comparable to that of the laser pulse rms length τ . We assume e.g. a laser pulse linearly polarized in y. The electric field can be approximated by the envelope of the laser electric field to

$$E_y(t) = E_0 \exp\left(-\frac{t}{2\tau^2}\right), \quad (1.29)$$

because the ADK theory averages over DC fields. The complete envelope field distribution of a Gaussian laser in TEM₀₀ mode is then

$$E_x(r, z, t) = E_0 \frac{w_0}{w(z)} \exp\left(-\frac{r^2}{w(z)^2}\right) \exp\left(-\frac{t}{2\tau^2}\right) \quad (1.30)$$

in a cylindrical coordinate system. $w(z) = w_0(1 + (\frac{z}{z_0})^2)^{1/2}$ is the beam waist at longitudinal position z and $z_0 = \pi w_0^2/\lambda$ is the Rayleigh length. Now the complete ADK ionization integral is

$$n_e(r, z, t) = n_0 \left(1 - \exp\left(-\int_{-\infty}^t W_{ADK}(E_x(r, z, t'))dt'\right)\right). \quad (1.31)$$

Figure (1.2) shows a plane of the ionization ration n/n_0 of laser-ionized He according to equation (1.31) at $t \gg \tau$. One can see, that sharp density transitions are created transverse to the laser pulse propagation direction. This detail will become important in section (1.9.3) and in the experimental part of the thesis as such sharp transitions are a convenient tool for the injection of electrons in wakes.

1.3 PWFA theory

1.4 The linear regime

Herleitung by esarey [7]

$$E_\xi = 4\pi \int_0^\xi \rho \xi' \cos(k_p(\xi - \xi')) d\xi \quad (1.32)$$

The transformer ratio $R_{\text{trans}} = \frac{E_{\max}^+}{E_{\max}^-}$ in PWFA is defined as the ratio of the maximum accelerating electric field behind the driving bunch, E_{\max}^+ , to the maximum decelerating E_{\max}^- electric field acting upon drive beam electrons. Experimentally the transformer ratio is comparably easy access-able if one assumes the acceleration length for the witness beam and deceleration length for the drive

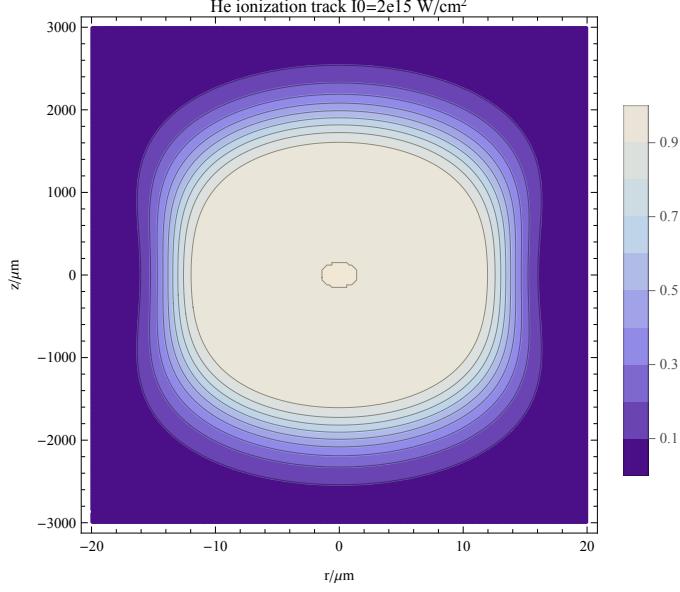


Fig. 1.2: He Ionization ratio by a 1 mJ Gaussian laser pulse with waist $w_0 = 20 \mu\text{m}$ and $\tau = 70 \text{ fs}$ FWHM pulse length

beam to be equal and that the witness beam is in accelerated at the peak accelerating field. Then it can be observed in the electron energy spectrum as the maximum energy gain of the witness beam divided by the maximum energy loss of the drive beam. In that sense the transformer ratio is a measure of efficiency with which the drive electron beam can transfer energy to the witness electron beam. In the linear regime for a Gaussian drive beam In [8] it is calculated and simulated that the transformer in the linear regime, which is otherwise limited to $R_{\text{trans}} \leq 2$ for a symmetric drive beam current profile [9], can reach up to $R_{\text{trans}} \approx 6.12$ by applying a triangular shaped drive beam current.

1.5 The blowout regime

Wavebreaking limit:

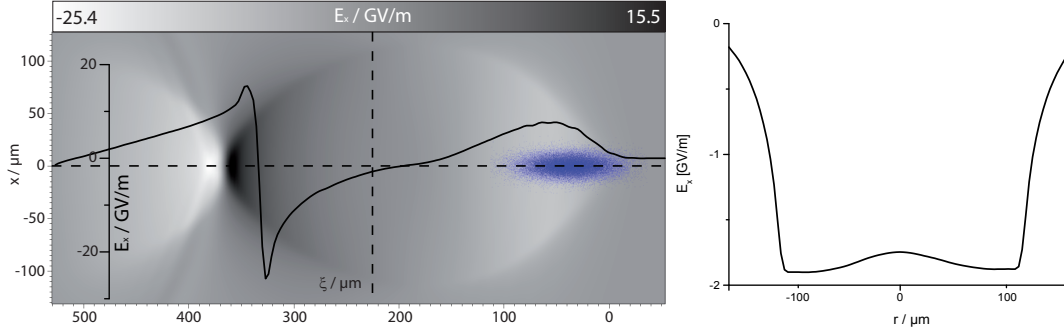
$$E_{\text{WB}} = cm_e \omega_P / q_e \simeq 96 \sqrt{n_e (\text{cm}^{-3})} \quad (1.33)$$

original paper: [10]

$$W_r = \partial_r W_z \quad (1.34)$$

1.6 Descriptions for the blowout regime

Lotov, Suk, breakdown of fluid theory Q-tilde and resonant wake excitation.



1.7 Physics of particle acceleration

In the previous chapters we examined the physics of the beam driven plasma wake excitation. The ultimate goal as presented in this work is to advantageously make use of the fields in order to inject and accelerate a high quality secondary electron beam, which is conventionally called the witness beam. If there are no substantial advantages between using the witness over the drive beam for a given application, it might not be worth the effort beyond a scholastic interest. In this section we will explain the basic electron beam behavior in an accelerator and from that determine the most important parameters.

1.7.1 Single electron dynamics

The analysis of the single particle dynamics in an accelerating structure by definition leaves out any interaction with other neighboring charges. This means that for now any space-charge effects are ignored and the trajectory in spatial and momentum space as a mere response to the accelerator is being considered. The 6D space, spanned by the spatial and momentum coordinates is called *Phase space* with phase space vectors Φ . In this work only linear accelerators are considered, with z being the direction of acceleration. The two projected subspaces transverse to z , are called transverse phase space or *trace space*.

The electron's equation of movement is completely described by the lorentz equation (1.5), which can be further simplified.

Similar to the assumptions made in par-axial optics the electron can be expected to follow a straight line with no change in momentum in the absence of any deflecting or accelerating force and any small change in that trajectory can be expressed as a finite number of linear changes. Also as in par-axial optics this gives the possibility to describe the electron beam trajectory with linear transformations, represented by a matrix formalism. This idea can be extrapolated to a linear

transformation of the entire phase space vector

$$\Phi_f = \hat{R}\Phi_i$$

$$\begin{pmatrix} x_f \\ x'_f \\ y_f \\ y'_f \\ z_f \\ \delta_f \end{pmatrix} = \begin{pmatrix} R_{11} & R_{12} & R_{13} & R_{14} & R_{15} & R_{16} \\ R_{21} & R_{22} & R_{23} & R_{24} & R_{25} & R_{26} \\ R_{31} & R_{32} & R_{33} & R_{34} & R_{35} & R_{36} \\ R_{41} & R_{42} & R_{43} & R_{44} & R_{45} & R_{46} \\ R_{51} & R_{52} & R_{53} & R_{54} & R_{55} & R_{56} \\ R_{61} & R_{62} & R_{63} & R_{64} & R_{65} & R_{66} \end{pmatrix} \begin{pmatrix} x_i \\ x'_i \\ y_i \\ y'_i \\ z_i \\ \delta_i \end{pmatrix} \quad (1.35)$$

as a conservative force acts upon it, with the spatial components x, y, z , the transverse momenta $x' = \frac{p_x}{p_z}, y' = \frac{p_y}{p_z}$ and the deviation $\delta = \frac{\delta p_z}{p_z}$ from the design momentum p_z . The matrix $\mathbf{R}_{m,n} = \frac{\delta \Phi_n}{\delta \Phi_m}$ is the Jacobian of this transformation and as that it requires $\det(\hat{R}) = 1$.

A good description of linear beam optics can be found in [11] or [12].

1.7.2 Liouville Theorem

When now considering an entire bunch of electrons it comes in handy to describe it as a smooth distribution $f(\vec{r}, \vec{p})$ in spatial (\vec{r}) and momentum (\vec{p}) coordinates. The entire

$$\int_{-\infty}^{\infty} f(\vec{r}, \vec{p}) d\vec{r} d\vec{p} = 1. \quad (1.36)$$

The Liouville Theorem states that if only conservative forces are applied to the bunch the total phase volume occupied by the distribution stays constant. This is mathematically equivalent to any transformation that maintains condition (1.36), which can be expressed by Jacobian transformations of the kind described by equation (1.35). Of course \hat{R} does not need to act upon the entire 6D-Phase space. In fact it is common to reduce the analysis and describe only changes in the trace space as the planes are mathematically independent and sometimes beam-optical devices do not change both trace space planes as e.g. dipoles.

In order to obtain a measure of the actual phase space volume the statistical moments of the distribution can be determined by evaluating the integral

$$\langle x^n \rangle = \int_{-\infty}^{\infty} f(\vec{r}, \vec{p}) x^n dx. \quad (1.37)$$

1.7.3 Courant-Snyder coefficients, brightness and emittance

Courant and Snyder in their summary paper [13] have set the standard for defining the phase space volume in the trace space with an ellipse equation for its boundary

$$\gamma \langle x^2 \rangle + 2\alpha \langle x \rangle \langle x' \rangle + \beta \langle x'^2 \rangle = \epsilon. \quad (1.38)$$

$$\alpha = \frac{\langle x^2 \rangle}{\epsilon}, \gamma = \frac{\langle x'^2 \rangle}{\epsilon}, \beta = \frac{\langle xx' \rangle}{\epsilon} \quad (1.39)$$

are the so called *Courant Snyder parameters* with $x' = \frac{p_x}{p_z}$ being the ratio between the transverse momentum p_x and the longitudinal momentum p_z . The constant of the ellipse ϵ is the trace space emittance. As $f(\vec{r}, \vec{p})$ is considered to be smooth function, it might as well consist of a distribution

that only approaches 0 so that it is difficult to draw a absolute volume edge as illustrated in figure (1.3). Because of this and for the sake of simplicity in comparing the value with experimental data, it is useful to work with the rms values. So the *rms trace space emittance* according to [14] is

$$\epsilon_{\text{tr,rms}} = \sqrt{\langle x^2 \rangle \langle x'^2 \rangle - \langle xx' \rangle^2}. \quad (1.40)$$

This can additionally be normalized to the *normalized rms trace space emittance* into the form

$$\epsilon_{n,\text{tr,rms}} = \frac{p_z}{m_e c} \sqrt{\langle x^2 \rangle \langle x'^2 \rangle - \langle xx' \rangle^2} \quad (1.41)$$

so that its value stays current during acceleration. The emittance is an important value, as it is invariant under conservative transformations and therefore an important figure of merit for electron beam quality in general. Definition (1.41) will mostly be applied in the context of this work. As

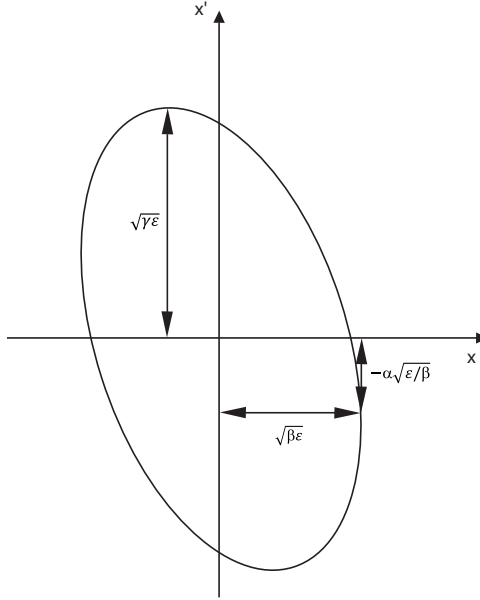


Fig. 1.3: Illustration of the trace space ellipse and its connection to the Courant Snyder coefficients.

in the forthcoming parts of this work we will have a look at numerical simulations conducted with particle-in-cell (PIC) Simulations, that handle discrete phase space points as electron beam representation instead od a continuum a discrete emittance expression will be used. For that the

electron beam moments are sums in the following form.

$$\langle x^2 \rangle = \frac{1}{n} \sum_{i=1}^n x_i^2 - \frac{1}{n^2} \left(\sum_{i=1}^n x_i \right)^2 \quad (1.42)$$

$$\langle x' \rangle = \frac{1}{n} \sum_{i=1}^n \left(\frac{p_{x,i}}{p_{z,i}} \right)^2 - \frac{1}{n^2} \left(\sum_{i=1}^n \frac{p_{x,i}}{p_{z,i}} \right)^2 \quad (1.43)$$

$$\langle xx' \rangle = \left(\frac{1}{n} \sum_{i=1}^n x_i \frac{p_{x,i}}{p_{z,i}} - \frac{1}{n^2} \sum_{i=1}^n x_i \sum_{j=1}^n \frac{p_{x,i}}{p_{z,j}} \right)^2 \quad (1.44)$$

1.7.4 electron bunch focussing

1.8 Electron Trapping in plasma accelerators

In order to derive an expression for the trapping condition of a single electron in PWFA, one has to start with the equation of motion for such a single electron.

$$\vec{F} = \frac{d\vec{p}}{dt} = q(\vec{E} + \frac{\vec{v}}{c} \times \vec{B}) \quad (1.45)$$

with the electron charge q electric field \vec{E} and magnetic field \vec{B}

This leads to the single particle electron hamiltonian

$$H = \gamma mc^2 + q_e \Phi \quad (1.46)$$

with the temporal derivative.

$$\frac{dH}{dt} = \frac{d}{dt}(\gamma m_e c^2) + \frac{d}{dt}(q\Phi) \quad (1.47)$$

$$= \vec{v} \frac{d\vec{p}}{dt} + \frac{d}{dt}(q\Phi) \quad (1.48)$$

$$= q\vec{v}(-\nabla\Phi - \frac{\partial\vec{A}}{\partial t}) + \frac{\vec{v} \times \vec{B}}{c} + \frac{d}{dt}(q\Phi) \quad (1.49)$$

$$= q(\frac{d}{dt}\Phi - \vec{v}\vec{\nabla}\Phi - \vec{v}\frac{\partial\vec{A}}{\partial t}) \quad (1.50)$$

$$= q(\frac{\partial\Phi}{\partial t} - \vec{v}\frac{\partial\vec{A}}{\partial t}) \quad (1.51)$$

If one assumes now, that the wake fields are constant during the trapping process, then

$$(\frac{\partial}{\partial t} + v_\phi \frac{\partial}{\partial z})f = f(z - v_\phi t) \quad (1.52)$$

$$(\frac{\partial}{\partial t} + v_\phi \frac{\partial}{\partial z})f = 0 \quad \forall f(\vec{r}, z - v_\phi t) \quad (1.53)$$

which is especially true for the hamiltonian.

$$\begin{aligned}\frac{d}{dt}H &= q\left(\frac{\partial\Phi}{\partial t} - \vec{v}\frac{\partial\vec{A}}{\partial t}\right) \\ &= -qv_\phi\left(\frac{\partial\Phi}{\partial z} - \vec{v}\frac{\partial\vec{A}}{\partial z}\right)\end{aligned}$$

Since $H - v_\phi P_z = \text{const.}$

$$H - v_\phi P_z = \text{const.} \quad (1.54)$$

$$\gamma mc^2 + \Psi - v_\phi p_z - v_\phi q A_z = \text{const.} \quad (1.55)$$

$$\gamma + \frac{q\Phi}{mc^2} - v_\phi \frac{p_z}{mc^2} = \text{const.} \quad (1.56)$$

$$\gamma - v_\phi \frac{p_z}{mc^2} - \underbrace{\frac{q}{mc^2}(\Phi - v_\phi A_z)}_{\bar{\Psi}} = \text{const.} \quad (1.57)$$

$\bar{\Psi}$ is the trapping potential, that determines the potential difference for an electron in a potential that moves with a phase velocity v_ϕ with respect to the laboratory frame. It is valid for small as for relativistic velocities. With the trapping potential one can calculate if an electron inside the plasma wake will be accelerated or not i.e. if electrons will be able to catch up with the wake's velocity during the propagation of the wake or if it will slip out of the potential. From the prior calculations a general formula can be determined, that compares

$$\Delta\bar{\Psi} = \bar{\Psi}_i - \bar{\Psi}_f = \gamma_f - \gamma_i - \gamma_f \frac{v_\phi v_f}{c^2} + \gamma_i \frac{v_\phi v_i}{c^2} \quad (1.58)$$

In order to honor the name "trapping potential" i.e. to apply this derivation to make predictions of the electron trapping behavior in the plasma wake, it is necessary to define a trapping condition. An obvious and conventional choice is that an electron should catch up with the wake's velocity so that $v_f = v_\phi$. Equation (1.58) consequently simplifies to

$$\Delta\bar{\Psi} = \gamma_\phi - \gamma_i - \gamma_\phi \frac{v_\phi^2}{c^2} + \gamma_i \frac{v_\phi v_i}{c^2} \quad (1.59)$$

Equation (1.59) can be further separated into different physical cases:

luminal wakefield, electron injected at rest

In this case the plasma wake travels with a phase velocity near the speed of light, which is the case for beam-driven scenarios with high γ driver beams ($v_\phi \approx c$), and electrons starting inside the wake initially at rest ($v_i \approx 0$). Here Equation (1.59) simplifies to

$$\Delta\bar{\Psi} = -1 \quad (1.60)$$

Examples of this case are the underdense photocathode, or Trojan Horse injection [15], or wakefield induced ionization injection [16].

luminal wakefield, electron injected with $v \neq 0$

In external injection schemes the electrons are already pre-accelerated when they are injected into the wake so that the trapping condition becomes

$$\Delta\bar{\Psi} = -\gamma_i(1 - \frac{v_i v_\phi}{c^2}) \approx -\gamma_i(1 - \frac{v_i}{c}). \quad (1.61)$$

subluminal wakefield, electron injected at rest

$$\Delta\bar{\Psi} = \gamma_\phi(1 - \frac{v_\phi^2}{c^2}) - 1 = \gamma_\phi^{-1} - 1 \quad (1.62)$$

This formula can for example be applied to ionization injection in LWFA [17] or beam-driven ionization injection schemes in which the wake's phase velocity is retarded such as the Downramp-assisted Trojan Horse (DTH) [18], which this work has as special focus on. In latter case mathematically strictly speaking $\frac{dH}{dt} \neq 0$, but for small changes $\frac{dH}{dt} \approx 0$ during the injection process of the electrons, equation (1.62) can still be applied.

superluminal wakefield

There are physical situations imaginable in which the wake or at least part of the wake move with a phase velocity faster than the speed of light. This is the case for example when a beam driven wake traverses an electron density upramp. From the previous deductions it seems obvious, that trapping electrons in such a superluminal wakefield is not possible, as γ_ϕ^{-1} becomes complex for $v_\phi > c$.

However, if the superluminosity is only transient as with a short density upramp, the phase velocity will return to c right after the transition. In this case trapping can be possible, but the mathematic tool presented in this section is insufficient to describe the trapping and the phase velocity after the transition is setting the demand on the potential.

1.8.1 Trapping position and bunch compression

Assuming that the longitudinal wake field $\frac{\partial E_z}{\partial r} = 0$ for a sufficiently wide radius the trapping behaviour can be seen in 1D only. In the blowout regime the acceleration gradient is to second order linear in ξ (compare section (1.5)) with

$$E_z(\xi) = \tilde{E}_0 \xi. \quad (1.63)$$

One should keep in mind that the origin of the coordinate system has been shifted so that $\xi = 0$ is at the zero-crossing of the electric field. \tilde{E}_0 is the slope of the accelerating field. This will be filled with values later on, but for now we are just interested in a more general derivation. Additionally equation (1.63) is only valid within the boundaries $[-\lambda_p/2, \lambda_p/2]$. Integrating equation (1.63) gives the potential

$$U_z(\xi) = \frac{1}{2} \tilde{E}_0 \xi^2. \quad (1.64)$$

Now equation (1.64) is inserted in equation (1.60) and rearranged in order to find for an electron released at an initial position ξ_i its trapping position ξ_f by deriving

$$\bar{\Psi}_f - \bar{\Psi}_i = -1 \quad (1.65)$$

$$U_z(\xi_f) - U_z(\xi_i) = -\frac{m_e c^2}{q_e} \quad (1.66)$$

$$(\xi_i^2 - \xi_f^2) = -\underbrace{\frac{2m_e c^2}{\hat{E}_0 q_e}}_{\alpha_t} \quad (1.67)$$

$$\xi_f = -\sqrt{\xi_i^2 + \alpha_t}. \quad (1.68)$$

Equation (1.68) is now the relation between release and trapping position of an electron in the co-moving frame for an accelerating field approximated to be linear. Merely negative values are considered, as a trapping only happens at the back of the wake. Forth going with our calculation we would like to handle a distribution of electrons to get closer to the description of the witness electron beam. This finding can then be used to calculate the compression of a released electron beam during the trapping. For that we start with a 1D spatial Gaussian distribution with rms length σ_ξ . We will later see that this assumption in fact resembles very well the distribution of interest.

$$f(\xi) = \frac{1}{\sigma_\xi \sqrt{2\pi}} e^{-\frac{(\xi+\delta_\xi)^2}{2\sigma_\xi^2}}. \quad (1.69)$$

The distribution should be normalized to

$$\int_{-\infty}^{\infty} f(\xi) d\xi \stackrel{!}{=} 1. \quad (1.70)$$

Equation (1.69) is now the initial injected electron beam and can, by applying equation (1.68) be used to calculate the trapped electron beam distribution.

$$f_f(\xi) = f(\xi_i(\xi_f)) \left\| \frac{\partial \xi_f}{\partial \xi_i} \right\| \quad (1.71)$$

$$= \frac{1}{\sigma_\xi \sqrt{2\pi}} e^{-\frac{(\sqrt{\xi_f^2 - \alpha_t} + \delta_\xi)^2}{2\sigma_\xi^2}} \frac{\xi_i}{\sqrt{\xi_i^2 + \alpha_t}} \quad (1.72)$$

$$= \frac{1}{\sigma_\xi \sqrt{2\pi}} e^{-\frac{(\sqrt{\xi_f^2 - \alpha_t} + \delta_\xi)^2}{2\sigma_\xi^2}} \frac{\sqrt{\xi_f^2 - \alpha_t}}{\sqrt{\sqrt{\xi_f^2 - \alpha_t}^2 + \alpha_t}} \quad (1.73)$$

$$= \frac{1}{\sigma_\xi \sqrt{2\pi}} e^{-\frac{(\sqrt{\xi_f^2 - \alpha_t} + \delta_\xi)^2}{2\sigma_\xi^2}} \frac{\sqrt{\xi_f^2 - \alpha_t}}{\sqrt{\xi_f^2 - \alpha_t + \alpha_t}} \quad (1.74)$$

$$= \frac{1}{\sigma_\xi \sqrt{2\pi}} e^{-\frac{(\sqrt{\xi_f^2 - \alpha_t} + \delta_\xi)^2}{2\sigma_\xi^2}} \frac{\sqrt{\xi_f^2 - \alpha_t}}{\sqrt{\xi_f^2 - \alpha_t + \alpha_t}} \quad (1.75)$$

$$= \frac{1}{\sigma_\xi \sqrt{2\pi}} e^{-\frac{(\sqrt{\xi_f^2 - \alpha_t} + \delta_\xi)^2}{2\sigma_\xi^2}} \frac{\sqrt{\xi_f^2 - \alpha_t}}{\sqrt{\xi_f^2}} \quad (1.76)$$

$$= \frac{1}{\sigma_\xi \sqrt{2\pi}} e^{-\frac{(\sqrt{\xi_f^2 - \alpha_t} + \delta_\xi)^2}{2\sigma_\xi^2}} \frac{\sqrt{\xi_f^2 - \alpha_t}}{\xi_f} \quad (1.77)$$

$$= \frac{1}{\sigma_\xi \sqrt{2\pi}} e^{-\frac{(\sqrt{\xi_f^2 - \alpha_t} + \delta_\xi)^2}{2\sigma_\xi^2}} \sqrt{1 - \frac{\alpha_t}{\xi_f^2}} \quad (1.78)$$

$$(1.79)$$

One should note here, that equation (1.78) as well as equation (1.69) offer positive as well as negative solutions due to the symmetry of the potential. Causality and the physics of accelerators does of course only allow solutions with $\xi_f < 0$. Since we assume that no charge is lost or created during trapping for $f_f(\xi)$ as well a normalization so that

$$\int_{-\infty}^0 f_f(\xi) d\xi \stackrel{!}{=} 1 \quad (1.80)$$

is required.

Equation (1.78) can be seen a response function to an electron release.

A complete description of velocity bunching as it occurs in wakefields is described in [19, 20].

1.9 Acceleration methods in PWFA

The strong accelerating fields in PWFA can be harvested with a variety of methods. They differ in experimental complexity and demand towards drive beam peak current.

1.9.1 External injection - Double bunch

External injection is the least complex PWFA setup and is also the method that has been demonstrated much earlier than other methods. The basic idea is that a plasma wake is set up by an electron beam, electrons - either from the same electron beam or by a trailing electron beam - are accelerated, if they are at the right phase with respect to the wake. Figure (1.4) depicts a sketch of a double-bunch PWFA in the blowout regime.

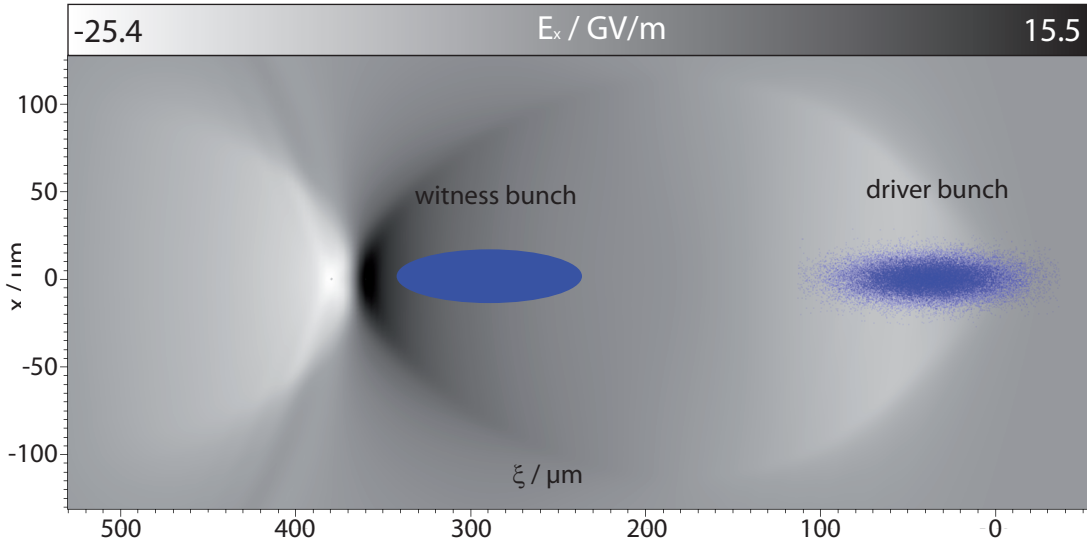


Fig. 1.4: Sketch of a double bunch acceleration. The driver electron beam excites a plasma wake, here in blowout regime and continuously loses energy due to the decelerating fields, while the electrons of the witness beam are trailing in the accelerating field gain energy

The first experimental realization of a PWFA was established in 1988 at the Argonne advanced accelerator test facility (AATF) [21]. With a method successfully applied to measure the wake fields in accelerating structures a $2 - 3$ nC electron beam with a rms bunch length of 2.4mm was used to drive a wake in a 33 cm long plasma at a density of the order of 10^{13} cm^{-3} . The driving bunch was trailed by a low-charge witness beam with variable delay to scan the wake fields. The oscillating nature of the wake fields was well measured with a maximum accelerating gradient of 1.6 MeV/m. With a higher driver witness beam charge of 4 nC [22] it was possible to show a non-linear wake with an accelerating gradient of 5.3 MeV/m.

In 2006 at the Final Focus Test Beam Facility (FFTB) at the Stanford Linear Accelerator Center (SLAC) the blow-out regime was finally reached as described in [23]. A 42 GeV electron beam with a spot size of $10 \mu\text{m}$ and rms bunch length of $15 \mu\text{m}$ propagated through a 85 cm Li oven. The shorter, high current bunch now allowed for driving a wake in a much higher plasma density of $2.7 \times 10^{17} \text{ cm}^{-3}$ in the blowout regime. Thanks to the extremely high wake field gradient of 52 GeV/m which effectively accelerated part of the electron beam to up to 85 GeV.

The successor experiment to the plasma experiments at the FFTB is the Facility for Advanced Accelerator Experimental Tests (FACET) [24]. Several double-bunch experiments have been successfully conducted. At FACET the double-bunches are produced by accelerating one long electron bunch all the way to the final chicane. While the chirped bunch is dispersed, the central part is cut out by a mask which results in a scrape in the current profile [25]. This method has the advantage that the transport of the beam along the LINAC is only required for one bunch. Efficiency and beamloading effects were studied in [26] and recently at FACET a double-bunch acceleration of positrons in a positron-driven wake was demonstrated by shaping the transverse plasma shape to a hollow channel, which effectively avoids any transverse fields that would otherwise defocus the positrons [27].

1.9.2 Density Downramp injection

As mentioned before the phase velocity of the plasma wake in PWFA is equal to the velocity of the driving electron bunch $v_\phi = v_{\text{bunch}}$ in the case of a constant plasma density, which is normally close to the speed of light. This feature of PWFA makes dephasing, which is the effect of the witness beam approaching the drive beam in the co-moving frame due to velocity differences between the bunches, mostly negligible. But it also complicates the injection of low-energy background plasma electrons into the wake. The injection can be made possible, by lowering the phase velocity. This is e.g. achieved when the driving bunch passes a region of negative plasma density gradient in beam propagation direction, a density downramp. Since the plasma wavelength λ_p (eq. 1.11), which is the characteristic scale of the longitudinal blowout length, depends on the plasma density the blowout must expand and contract on a density downramp or upramp respectively.

The phase position of the wake is

$$\phi = k_p \xi \propto \sqrt{n_e} \xi \quad (1.81)$$

in the co-moving frame with $\xi = z - ct$.

The phase velocity on a density gradient is

$$v_\phi(\xi, z) = -c \frac{\frac{\partial \phi}{\partial(ct)}}{\frac{\partial \phi}{\partial z}} \quad (1.82)$$

$$= \frac{\left(\frac{\partial k_p}{\partial t} \xi + \frac{\partial \xi}{\partial t} k_p \right)}{\frac{\partial k_p}{\partial z} \xi + \frac{\partial x}{\partial z} k_p} \quad (1.83)$$

$$= \frac{ck_p}{k_p \frac{1}{2n_e} \frac{\partial n_e}{\partial z} \xi + k_p} \quad (1.84)$$

$$= \frac{c}{\frac{1}{2n_e} \frac{\partial n_e}{\partial z} \xi + 1} \quad (1.85)$$

In [28] the injection of electrons into the second trailing plasma wake from wave breaking on a density downramp longer than the plasma wavelength was studied.

Injection into the first trailing plasma wake in PWFA from sharp density transitions has been studied by Suk et al. [29]. With an 1D hamiltonian analysis and simulations they found as injection criteria for a linear density downramp with a scale length $L_s = \frac{n_e}{\partial n_e / \partial z}$

$$k_p L_s < 1. \quad (1.86)$$

In [30] this description was refined and wave breaking as a criteria for injection was applied and injection of electrons originating from the high density region was observed.

These works do not consider the highly nonlinear blowout regime in which wavebreaking and trajectory crossing of sheath electrons naturally occurs, even for a flat plasma density profile. This means that in blowout regime even for rather smooth density gradients trapping of sheath electrons is possible. Grebenyuk et al. investigated the density downramp injection capabilities specific for the drive electron beam at the FlashForward facility [?]. They showed successful injection in PIC simulations for a drive beam of 2.5 kA peak current and at $k_p L_s \approx 3.3$ [31] and little dependence of witness beam properties on downramp length variation when keeping the density gradient constant.

The interplay between drive beam current, sheath electron energy at the vortex and wake potential is what determines the trapped charge and witness beam properties in this regime and is matter of ongoing research.

Experimental realization of injection due to a density downramp has been successfully applied in laser driven wakefield acceleration [32–34]. The first experimental realization in PWFA with an optically generated plasma density spike is part of this thesis. The concept is described here and the experimental results can be found in chapter 2.

1.9.3 Plasma Torch

In laser-driven plasma wakefield acceleration schemes density gradients are normally generated hydrodynamically for example with razorblades or knife-edges as gas flow obstacles that are positioned on top of gas jets [35, 36]. Relying on hydrodynamic gradients is necessary, because the high electric fields of the driving laser pulse is normally capable of ionizing the medium in which it excites the wake. A pure electron density gradient generated prior to the laser pulse would be non-existing after the driving laser-pulse. This

In contrast to these hydrodynamic methods we have investigated the optical generation of a plasma density spike, also called *Plasma Torch* [37, 38] as means for an electron bunch injection. In PWFA for exciting a plasma wake in blowout regime neither the electron bunch electric field nor the wake fields need to be so strong that they ionize He. Therefore the electron density shape can be determined by laser pulses, ionizing gas prior to the arrival of the driving electron bunch. The shape can be expected to be maintained over the plasma recombination time which is on the order of a few ns . Therefore picosecond control over relative time of arrival between electron beam and laser pulses is already sufficient to make sure that the electron bunch propagates through the desired density profile. A mixture of Hydrogen and Helium gas with its ionization gap (see figure 1.1) is convenient for the distinct generation of a density spike. Figure (1.5) demonstrates a sketch of the proposed setup. A pre-ionization laser pulse ionizes a long plasma column and only ionizes the Hydrogen gas to a homogeneous plasma along the electron beam orbit. A split-off laser arm, separated by a beam splitter, is focused down transverse to the beam orbit with higher intensity to ensure full He ionization in a confined region. Both laser arms need to ionize the gas prior to the electron beam. Due to the exponential dependence between ionization rate and electric field density downramps on the order of $10\mu m$ length can be formed and precise timing control ensures these profiles are contained until the electron beam arrives. The gradients can be tuned very easily by changing the relative gas density of hydrogen and helium. For a gas density

In [37] and [38] we used FACET-like driver bunches

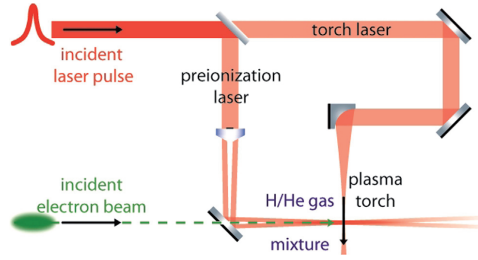


Fig. 1.5: Sketch of Plasma Torch injection setup [38].

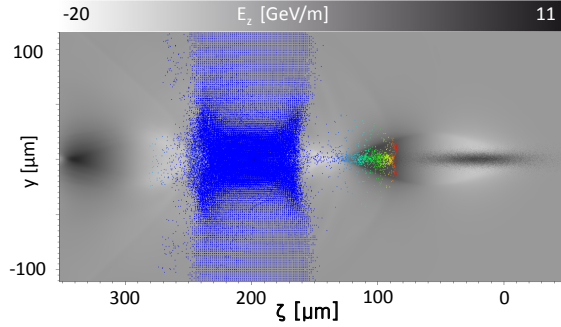


Fig. 1.6

1.9.4 ionization injection

In all previously outlined injection types, electrons to be accelerated in the wake are at a nonzero velocity when injected, which is an advantage as regards the requirements on the wakefield gradient. Ionization injected electrons are in a bound state until they are released to continuum inside the wake. This from a physics standpoint requires the plasma to only be partially ionized when the wake is excited and from an engineering stand point ionization levels that are sufficiently distinct in their ionization rates to ensure a controlled ionization. We will further use the term Low ionization threshold (LIT) medium for the part to be ionized in order to drive the wave in it and High ionization threshold (HIT) medium for the part that originates the injected witness beam electrons. Of course, HIT and LIT medium can be the same, by making use of different ionization levels. If, however, HIT and LIT are different gases as e.g. H₂ and He, their gas density ratio becomes a handy degree of freedom to control the injected charge. Experimentally in [39] ionization ionjection was shown in a Rb oven. The electron beam head electric fields were used to ionize Rb → Rb⁺, while the drive beam tails' field overlapped with the wake electric fields were strong enough to ionize Rb⁺ → Rb²⁺

and inject the electrons. This method of injection is conceptually comparable to ionization injection, where the driving laser pulse fields are strong enough to ionize several ionization levels with injection at the back of the laser or in other words the front of the wake [40].

In [41] and [16] with theory and simulations a setup was examined where only the back of the wake had sufficiently high fields to ionize the HIT medium and combined with the concept of the trapping potential as described in section (1.8). It could be shown that the combined requirements for trapping, i.e. the overlap of the ionization region and the trapping region, confine the possible electron source which enables the generation of low emittance electron beams ($\epsilon_x = 1.5 \mu\text{m}$)

1.9.5 Trojan Horse injection

The underdense photocathode or Trojan Horse injection is one of the most complex injection techniques. It was proposed by B. Hidding in [15]. Neither the wake nor the beam electric fields are sufficient to ionize the HIT medium. Instead this is the duty of an additional short-pulse laser pulse, trailing the driving electron beam. Given full control over laser-to-electron beam alignment and synchronization, it is possible to ionize and release electrons wherever in the wake it deems necessary. It could be shown that a release in the potential minimum, i.e. the zero-crossing of the wake is particularly advantageous, because the electron acceleration to relativistic speed is extremely rapid ($\approx \frac{\lambda_p}{2c}$) and the bunch compression is maximum at this injection position. Furthermore the emittance of Trojan Horse injected electron beams can be very low on the order of a few $\epsilon_{\text{rms}} \approx 10^{-8} \text{ mrad}$. The reasons for that lie to one part in the ionization method. A typical 800 nm Ti:Sa few fs laserpulse only needs a peak intensity of 10^{15} W/cm^2 to ionize a HIT medium as e.g. $\text{He} \rightarrow \text{He}^+$. The normalized vector potential $a_0 = \frac{q_e E_0}{m_e c^2} = 0.022 \ll 1$ implies that no ponderomotive force can be expected that would impose an initial transverse momentum to the released electron bunch so that the transverse momentum is basically determined by the HIT gas temperature. A detailed theoretically supported PIC simulation parameter scan in [42] examined scalings between witness emittance and brightness and laser beam parameters as beam waist w_0 , pulse length and peak intensity. An indifference towards pulse length as well as an emittance increase with w_0 and intensity was found.

In [43] a detailed comparison between laser and electron beam driven wakefield acceleration is drawn out.

1.10 Trapping behaviour for the Trojan Horse Injection

1.10.1 The role of the ionization front

We saw in section (1.8.1) that the length and position of the originally released electron bunch as well as the accelerating gradient plays a significant role for establishing an effective velocity bunching. In the Trojan Horse injection concept it is possible to inject electrons at a phase of choice. We want to examine now what kind of initial electron bunch distributions we can expect. For that we start with a 1D consideration. We combine this with the information from section (1.2.2) and will

Figure (1.7) demonstrates the time-dependent ionization ratio in He during the propagation of a 100 fs long laser pulse with peak intensity $1 \times 10^{15} \frac{\text{W}}{\text{cm}^2}$ peak intensity , according to equation (1.31). The ionization front is clearly visible as a rapid increase of the ionization ratio. In [44] the structure of the ionization front of short-pulse lasers in He has been measured with single-shot supercontinuum spectral interferometry. They had a well-known chirped low-intensity probe laser

pulse co-propagating with the ionizing laser pulse. Interferometry of the spectrally dispersed probe pulse then revealed the length of the ionization front. Their results have demonstrated a very good agreement with the ionization front as predicted by the ADK formalism.

From that we can calculate the initial electron release distribution

$$f_i(\xi) = \frac{d}{dt} n_0 \left(1 - \exp \left(- \int_{-\infty}^t W_{\text{ADK}}(E_x(r, z, t')) dt' \right) \right) \quad (1.87)$$

$$= n_0 \frac{d}{dt} \exp \left(- \int_{-\infty}^t W_{\text{ADK}}(E_x(r, z, t')) dt' \right). \quad (1.88)$$

Two things are important to notice:

1. The ionization front and with that the initial release is much shorter than the actual laser pulse.
2. The center of the release electron distribution does not need to coincide with the center of the laser pulse.

We now want to further investigate on the initial electron release distribution and how it depends on laser peak intensity and pulse lengths.

1.10.2 Dark current mitigation

Simulation

[45]

Experiment

1.10.3 Downramp assisted Trojan Horse

1.11 numerical modeling of Trojan Horse injection

1.11.1 emittance growth from space charge

1.11.2 Laser parameter variations

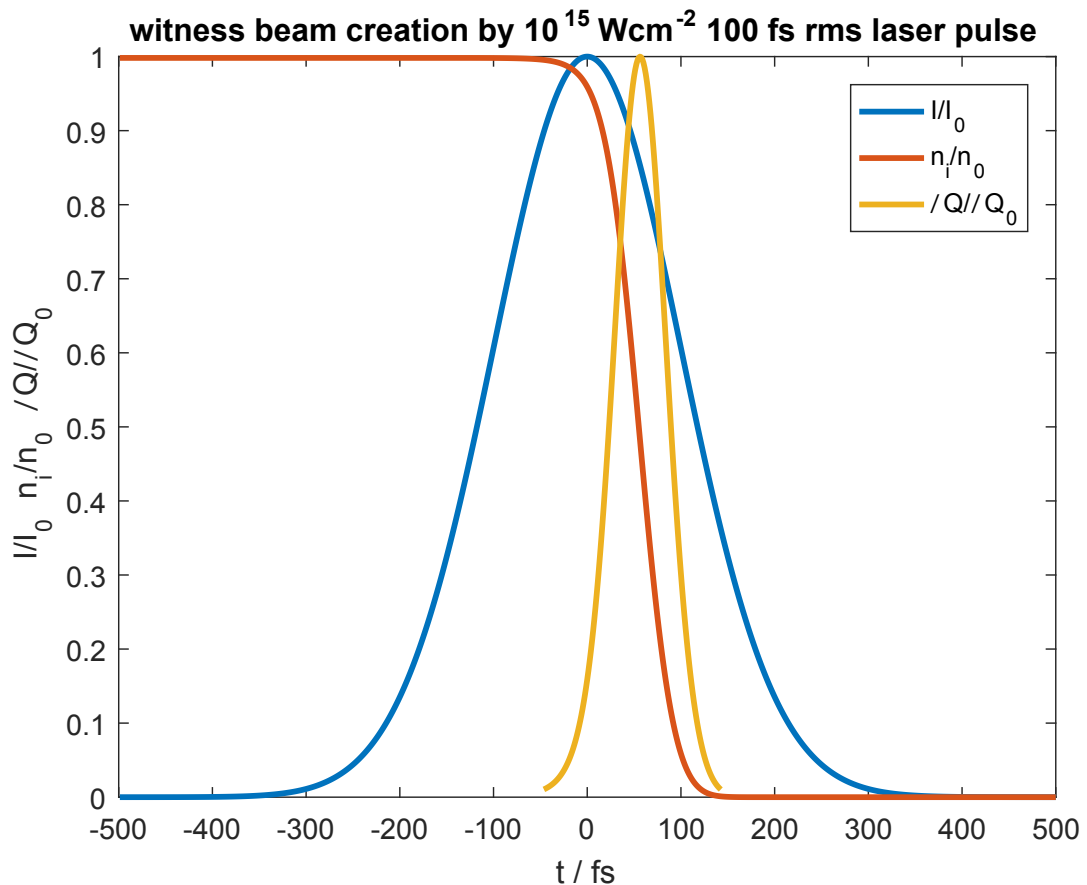
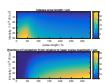
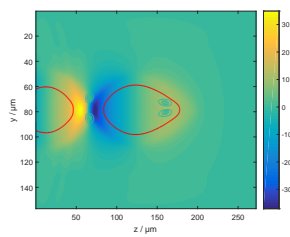
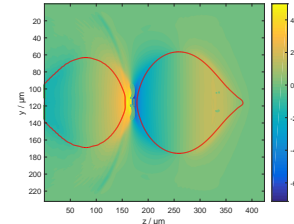
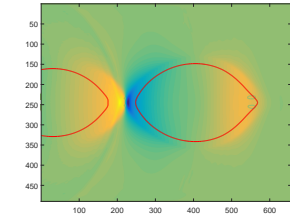


Fig. 1.7: Ionization front from a





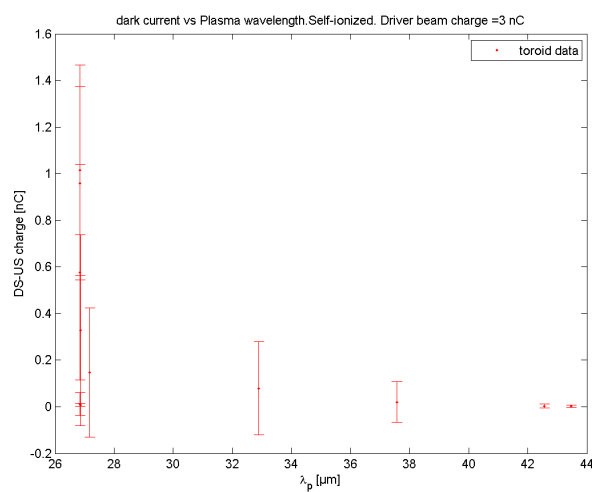


Fig. 1.8: Experimental evidence of dark current reduction in beam-ionized plasma

2. EXPERIMENT

In 2014 the experimental campaign for demonstrating the proof-of-concept of Trojan Horse injection (see 1.9.5) started at the Facility for Advanced Accelerator Experimental Tests (FACET) at the SLAC national laboratory as the experiment E210. It was a collaborative effort with researchers from the University of Hamburg, University of California Los Angeles (UCLA), University of Strathclyde Glasgow and Radiabeam technology with a devoted support from the SLAC personnel. The FACET experiments had to be designed to be non-excluding, which led to a fruitful joint learning process between several groups. It is fair to say that E210 was one of the most complex and accuracy-wise most demanding experiments conducted so far at FACET. Several steps were required in improving the overall setup, until the experiment was eventually successful. The most crucial obstacles to overcome were timing and alignment between two laser arms and the electron beam. The timing requirements between the electron beam and the pre-ionization laser are rather soft as long as the pre-ionization occurs before the arrival of the electron beam and with a timing difference less than the recombination time (ns-s range). However, proper control over relative time-of-arrival between the injection laser and the electron beam required - in principle - control over timing on the order of 10 fs. With an expected timing jitter in the range of 200 fs the best solution here was to accurately measure the relative TOA with an electro-optical sampling (described in 2.2) to determine the injection properties from the data, rather than hope for live-control. For finding the synchronization (t_0) as well as fine-alignment between electron beam and injection laser, a newly observed effect on the plasma glow described in 2.4 was measured and applied.

2.1 *The FACET experimental setup*

2.1.1 *LINAC*

2.1.2 *The FACET laser system*

Good description of FACET laser system in [46]

2.1.3 *E210 setup*

2.1.4 *Imaging spectrometer*

The imaging spectrometer consists of a dipole and three

2.1.5 *Laser energy calibration*

The FACET laser system ... The energy that can be used on target of the OAP is controlled at two points in the laser-beamline. At each point a cube-polarizer is surrounded by two $\lambda/2$ -waveplates, where the upstream one is motorized. The main energy waveplate is located in the laser-room

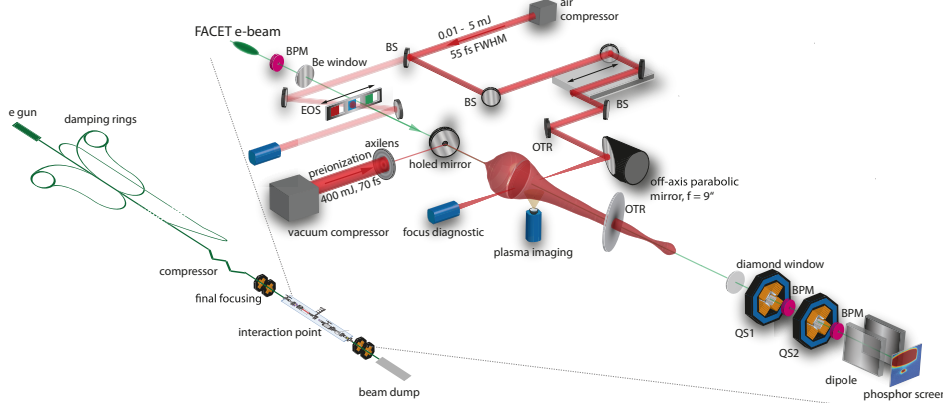


Fig. 2.1

and the probe-energy waveplate is located in the tunnel area shortly after the split between main laser path and probe laser path at the main sampler, which means that the probe laser energy is determined by both waveplate settings while the main laser energy is set by the main laser energy waveplate only. From the power-meter in the laser-room, that measures shot-by-shot laser pulse energy, all the way down to the tunnel a variety of optical components are used until the laser is finally focused onto the target. The typical shot-to-shot laser energy jitter is $\approx 5\%$ FWHM.

Manta Cameras: [47]

All measured losses in optical components combined with the fitted functions for the waveplate energies (see figure 2.2) combined give the on target energy applicable by axilens and OAP respectively.

$$\begin{aligned} W_{\text{Laser}}^{\text{OAP}} &= W_{\text{Laser}}^{\text{Laserroom}} \times 1.25 \times 10^{-2} \\ &\times (0.994 \cos^2((\phi_{\text{pol}}^{\text{main}} - 5.11^\circ)) + 6.16 \times 10^{-3}) \\ &\times (0.998 \cos^2((\phi_{\text{pol}}^{\text{probe}} - 17.8^\circ)) + 1.65 \times 10^{-3}) \end{aligned}$$

$$W_{\text{Laser}}^{\text{Axilens}} = W_{\text{Laser}}^{\text{Laserroom}} \times 0.253 \quad (2.1)$$

$$\times (0.994 \cos^2((\phi_{\text{pol}}^{\text{main}} - 5.11^\circ)) + 6.16 \times 10^{-3}) \quad (2.2)$$

$$(2.3)$$

This means that for a typical laser energy output of 500 mJ a maximum energy of 6.2 mJ on OAP target and 125.9 mJ on axilens could be used.

Energy limitations

$$E e^{-i(\omega t - kx)} = E e^{-i\omega(t - \frac{x}{c}(n_0 + n_2 I))} \quad (2.4)$$

The maximum energy that can be applied for the OAP ionization is additionally limited by the damage threshold of the windows. Three

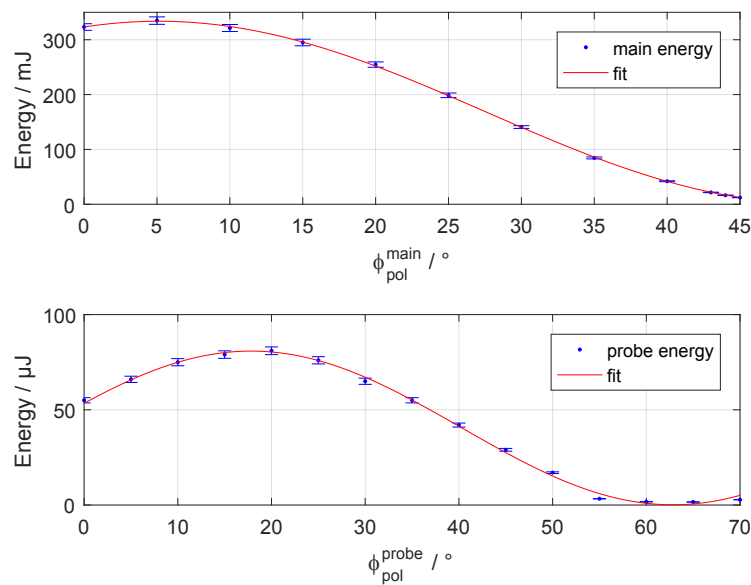


Fig. 2.2: Laser energy calibration for main energy waveplate (upper plot) and probe energy waveplate (lower plot)

1. Intensity
2. The Fluence damage threshold for a 560 fs 248 nm laser pulse is measured [48] to be $1.70 \frac{J}{cm^2}$. Measurements with a 55 fs 800 nm laser pulse in [49] indicate that the threshold is lower than $2 \frac{J}{cm^2}$
3. Nonlinear effects: B_{j1}

$$B = \frac{2\pi}{\lambda} \int_0^x n_2(x') I(x') dx' \quad (2.5)$$

The injection laser is coupled into the OAP chamber through a 3 mm thick MgF_2 window with an anti-reflection coating. By having the OAP in vacuum, more freedom of alignment is possible and focusing through a window is avoided, which could otherwise distort the laser focus or induce damage to the mirror. MgF_2 is the material of choice because of its low nonlinear refractive index value of $n_2(MgF_2) = 0.763 \times 10^{-16} \frac{cm^2}{W}$ [50]. The injection laser transverse profile can be approximated by a flat-top with a beam diameter of 10 mm. Then the energy maximum for $B = 1$ is 24.1 mJ. That corresponds to a Fluence of $30.6 \frac{mJ}{cm^2}$ and an intensity of $5.6 \times 10^{11} \frac{W}{cm^2}$

Timing jitter estimate

In order to establish a controlled injection of electrons into the wake, a synchronisation between electron beam and laser pulse on the order of few 10th of fs is desirable. The Vitara-T laser main oscillator is mode-locked to the master reference of the radio-frequency (RF) master reference [46]. This lock according to [46] has a timing jitter of

$$\sigma_t^{RF,laser} = 70 \text{ fs.} \quad (2.6)$$

The electron bunch on the other hand has a timing jitter with respect to the RF, which can be estimated with linear beam-optics as described in equation 1.35. Due to energy-dependent path lengths in the W-chicane the electron beam energy jitter translates into a timing offset with the relation

$$\sigma_t^{e^-,RF} \approx \Delta z_f/c \quad (2.7)$$

$$= R_{56} \delta_i/c. \quad (2.8)$$

The sector 20 chicane R_{56} is typically set to -7 mm to achieve maximum bunch compression and the rms energy jitter has been measured to be $\delta_i = \frac{18.7 \text{ MeV}}{20.35 \text{ GeV}} = 9.2 \times 10^{-4}$ [27] so that the rms time of arrival jitter of the electron beam with respect to the master RF reference can be estimated to be

$$\sigma_t^{e^-,RF} \approx 21.5 \text{ fs.} \quad (2.9)$$

Additional laser time-of-arrival jitter due to pointing jitter is small enough that its' contribution can be ignored. This leaves us with a total estimated laser pulse to electron time-of-arrival jitter of

$$\sigma_t^{e^-,laser} = \sqrt{(\sigma_t^{e^-,RF})^2 + (\sigma_t^{RF,laser})^2} = 73.2 \text{ fs.} \quad (2.10)$$

Keeping in mind that this is a rather optimistic estimate and long-term drifts might need adjustment to find the right timing such a jitter value requires a direct measurement of the relative TOA.

2.2 Electro Optical Sampling (EOS)

Electro-optical sampling is a method that is perfectly suited for determining such time-differences in Time-of-arrival between a laser-pulse and a Thz-source, as e.g. an ultra relativistic electron-beam, by exploiting the properties of optically anisotropic crystals and has been shown to be able to measure sub-picosecond electron bunches [51].

Electromagnetic waves, propagating through anisotropic crystals perceive a difference in dielectric permittivity ϵ_r , depending on entrance angle and polarization of the wave, which is why in a more general way the dielectric properties need to be addressed with the dielectric permittivity tensor $\hat{\epsilon}$. This is equivalent to a polarization-depending index of refraction, a property known as birefringence, which leads to a polarization-dependent phase velocity of light inside the crystal. A laser at the correct incident angle with respect to an anisotropic crystal will therefore notice a phase shift between different planes of polarization which leads to an overall change in the laser polarization, depending on the phase shift strength and the crystal size. Electro-optical crystals change the orientation of the dielectric permittivity tensor when an external electric field $\vec{E}_{\text{ext.}}$ is applied. The strength of this effect can be illustrated by taylor-expanding the impermeability tensor

$$\hat{\eta} = \hat{\epsilon}^{-1} \quad (2.11)$$

for small external electric fields $\vec{E}_{\text{ext.}}$ to

$$\eta_{ij} = \eta_{ij}(0) + r_{ijk}E_k + s_{ijkl}E_kE_l + \dots . \quad (2.12)$$

The linear dependency on the electric field strength is called Kerr-effect with r_{ijk} being the Kerr-coefficient. The Pockels effect with the Pockels coefficient s_{ijkl} describes quadratic dependency. In the context of this work and the described experiment only two electro-optical crystals were used, GaP and ZnTe. As both of them are packed in a zincblende geometry, which does not obtain an inversion center, the electro-optic effect is dominated by the Pockels-effect.

EOS setup

In order to measure the relative time-of-arrival between electron bunch and laser pulse an Electro optical sampling (EOS) was set up as a non-destructive shot-by-shot diagnostic.

In this experiment the crystal is located in close proximity (few mm distance) to the electron beam axis. Due to the high $\gamma_b \approx 42000$, the beam electric field is strongly lorenz-contracted and can be assumed to temporally only extend for the length of the electron beam. Consequently the electric field applied to the crystal and with that the induced birefringence are only active while the electron beam passes by the crystal. Figure 2.3 depicts the setup. A linear polarized laser pulse (red), a pickup of the probe beam, traverses the crystal with an angle of 45° with respect to the electron beam axis (green). The laser beam is collimated with a transverse diameter of 1cm and completely illuminates the crystal. For a better signal-to-noise ratio, an additional polarizing filter was installed prior to the picnic basket chamber. After the chamber follows a cross-polarized filter, which can remotely be rotated for alignment purposes.

During the measurement only the polarization of that transverse part of the laser which propagates through the crystal at the very moment in which the electron beam' electric field induces the birefringence will be rotated and not be filtered by the polarizing filter further downstream the laser beam path. As a result the signal has the form of a line as seen in figure 2.4 with a horizontal position linearly corresponding to the relative TOA.

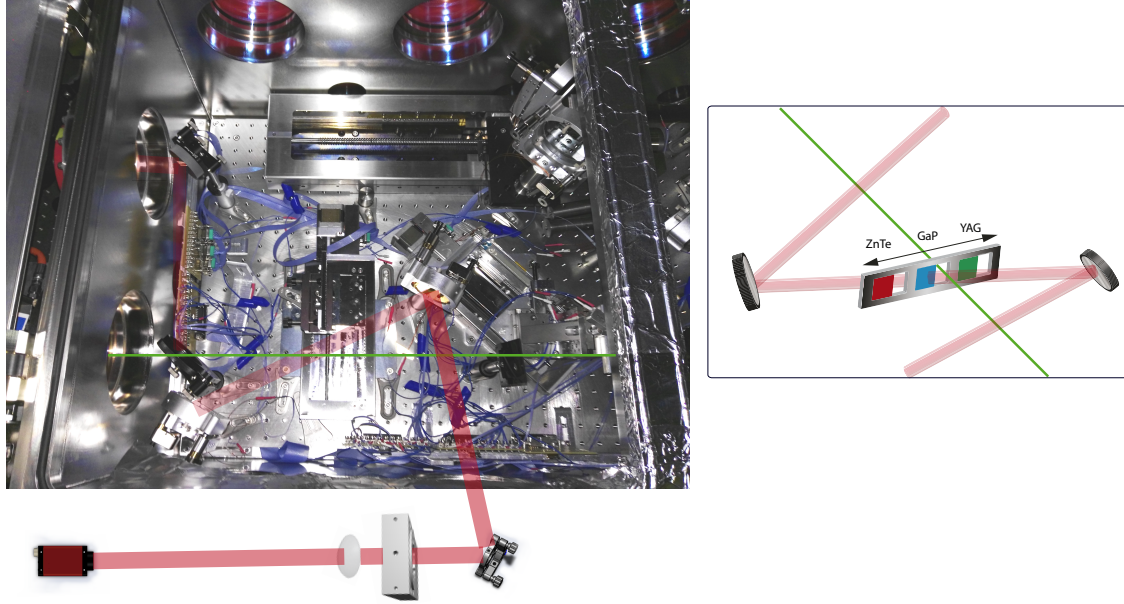


Fig. 2.3: Setup of upstream electro-optical sampling inside the picnic basket chamber. Electron beam (green) and EOS laser (red) co-propagate in a small angle

The crystal plate is oriented perpendicular to the electron beam axis to minimize temporal overlap and the laser has an ≈ 40 degree angle with the electron beam which enables a correlation between signal position i.e. the part of the laser with rotated polarization and relative timing.

The entire ladder supports a YAG crystal to find the electron beam axis, a 500 m thick ZnTe for broad timing scans and GaP with 100 μm thickness for fine resolution. A detailed description of the physics involved in the application of electro-optical crystals as TOA and bunch length diagnostic can be found in [52].

EOS calibration

The EOS signal can be seen in figure (2.4). A small region of interest of the raw images (a,d) is rotated and the background, which mostly consists of the laser profile is subtracted (b,e). The image projection shows a strong, but broad signal for the thick ZnTe crystal (c). The GaP signal is much cleaner. The Maximum position as well as a Gaussian fit is calculated to determine the relative timing. The EOS calibration was performed by changing the laser target time with respect to the RF main reference. For every time step several shots are performed to even out the timing jitter. We assume here that there is a timing jitter that behaves equally for every step in the data acquisition so that for a sufficient number of shots per time step the calibration becomes accurate. Taking too large datasets takes more time that drifts start to play a role. Therefore calibration result may vary from dataset to dataset. Furthermore calibration may vary from day to day due to deviation in laser alignment.

An EOS calibration is shown in figure (2.5) with a clear linearity between signal position an

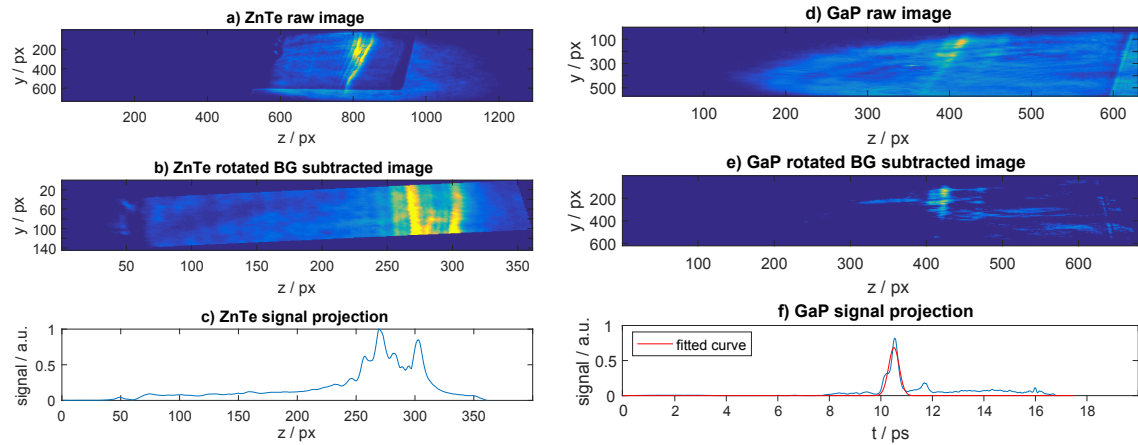


Fig. 2.4: EOS signal

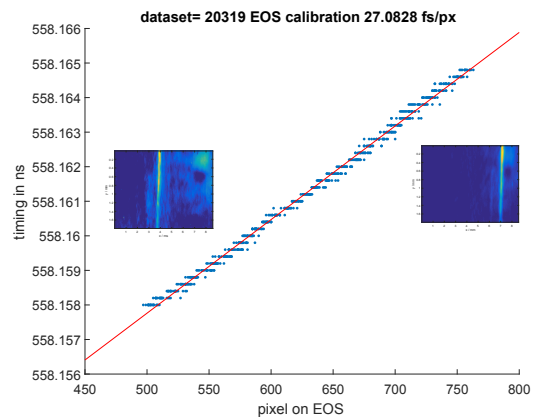


Fig. 2.5: Typical EOS calibration

timing as well as a slim scattering of the datapoints around the mean step value. In principal such a calibration is not required with this method prior to performing timing scans for the sake of the actual experiment. As long as sufficient datapoints are taken per step a calibration can be obtained specific for any such dataset, which led to a multitude of calibration data. Taking into account several timing scans over several days we can conclude a mean calibration with confidence interval

$$t_{\text{EOS}}^{\text{calib}} = 25.8 \pm 2.5 \frac{\text{fs}}{\text{px}}. \quad (2.13)$$

Measurement of the TOA timing jitter

With the calibrated EOS diagnostic one can now determine the actual relative timing jitter between electron beam and laser pulse and compare it with our estimate. Taking 1000 consecutive shots gives a measured timing jitter of

$$\sigma_t^{\text{TOA}} = 150.61 \pm 14.59 \text{ fs}. \quad (2.14)$$

This result shows that the previous estimate was indeed much too optimistic and that implementing the EOS diagnostic is a crucial tool to determine the shot-by-shot relative timing. One might now think about using this diagnostic now to pin down precisely the most predominant contributor to the timing jitter, which would have been a viable endeavor and could help in terms of stability. Thanks to the possibility to measure the timing shot-by-shot and non-invasive there was no need for this. The EOS gives us the freedom to operate and measure independent of the complex combination of short-term jitters long-term drifts, klystron malfunctions and the electron beam operation , which constantly requires small manual adjustments in order to maintain electron beam compression and alignment.

Moreover it gives is the possibility to sort our data by timing and investigate the physics depending on relative timing on a timescale of ≈ 30 fs. This sorting of data does not necessarily require an established calibration or any understanding about the current situation of the LINAC, as long as there is beam. The mere relative position of the EOS signal between different data points is sufficient for a sorting by time-of-arrival.

2.3 Ionization test

2.4 Plasma glow diagnostic

Section (2.2) describes the EOS commissioning and demonstrates that it is excellently suited for relative time-of-arrival measurements of electron beam an laser pulse. However, there is one detail, the EOS as it is set up is not capable of answering, which is at which timing or range of timing electron beam and injection laser pulse do spatially overlap, so that they are in synchronization. Luckily it was observed before at FACET that the plasma light emission increased significantly if it was not only ionized by the laser, but also afterwards hit by the electron beam.

Because this could be a potential solution to the synchronization problem we planned and performed a preparatory experiment to determine the time scales and physics of this transition. One huge advantage of the hydrogen FACET setup compared to the oven setup was that now several view ports allowed for observing the interaction. We set up a camera, observing cube 3 from bottom up and attached two band-pass filters on remote controllable flippers to it, one for

656 ± 10 nm and one filter for ... nm. The camera takes an integrates image over several μs , a time window, much larger than the plasma recombination time. The EOS then allows for sorting these images by TOA and measuring precisely the time scales.

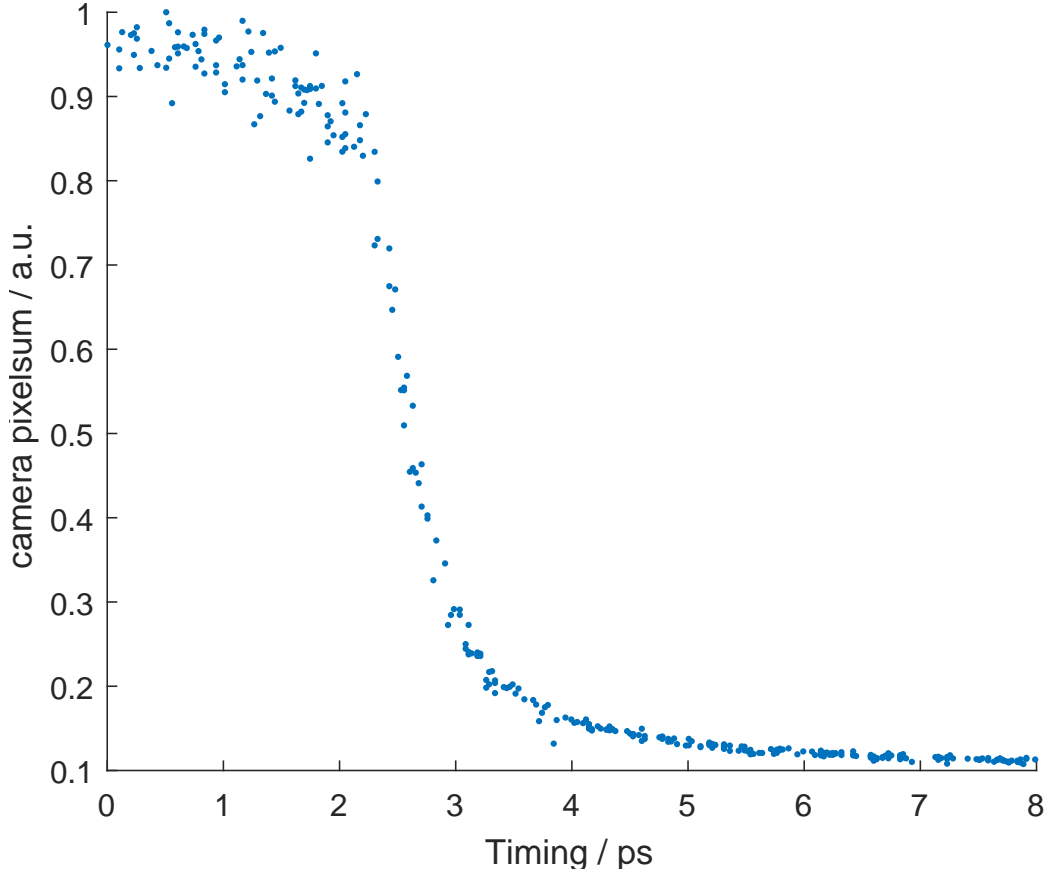


Fig. 2.6: Relative electron beam to injection laser timing scan. The pixel counts measured by the cube 3 vertical camera with a 656 ± 10 nm band-pass filter are sorted by the EOS. evaluation.

Figure 2.6 shows the plasma glow accumulated intensity at the wavelength 656 ± 10 nm, sorted by relative time-of-arrival between electron beam as measured by the EOS. The transition between a situation where the injection laser arrives earlier than the electron beam and vice versa is around 1 ps wide, which sufficiently fulfills the requirements to find a range of synchronization as the total range of the EOS crystal is around 20 ps ????. During the data acquisition the electron beam charge was 3.1 ± 0.17 nC.

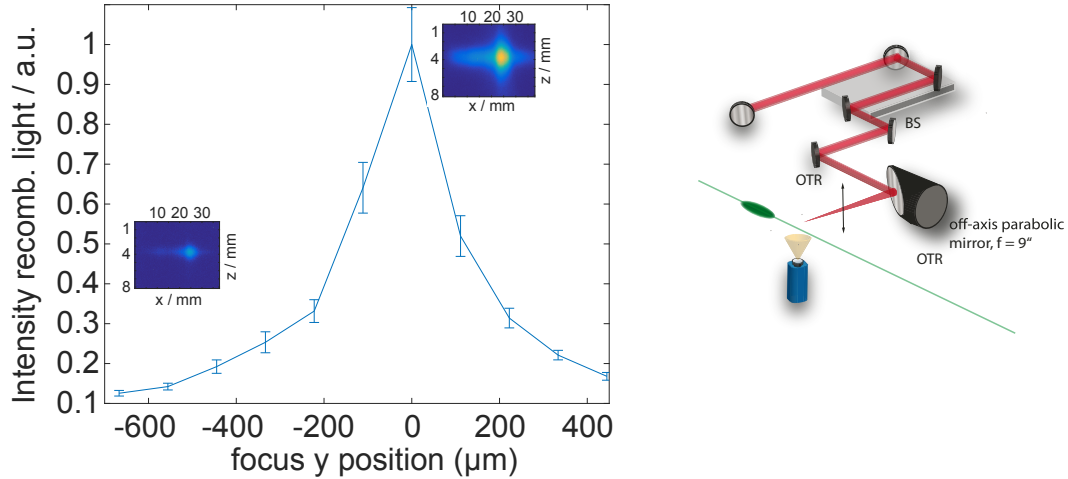


Fig. 2.7: Plasma glow in 7.8 torr H₂ ($n_e = 5 \times 10^{17} \text{ cm}^{-3}$) measured by vertical camera in cube 3. The injection laser off-axis parabola roll is scanned. The vertical plasma position is evaluated by the focus diagnostic.

2.5 Charge calibration

The witness beam charge is measured with two different methods, by comparing the total charge before and after the plasma section and from the intensity of a scintillating screen at the spectrometer.

Toroidal Current Monitors (toroids) before and after the plasma section seem to be the obvious diagnostic tool for additional charge. There are two reasons, however, why in this thesis the charge difference measured by the beam position monitors(BPMs) will be used instead. The first reason is that the toroids after the plasma section seemed to be vastly over-estimating the additional charge. Acceleration of several nanocoulomb in the plasma wake as sometimes given out by the toroids is, although maybe not impossible, hard to believe, especially when the BPMs show much more believable values. The thinking here is, that a direct hit of the toroid's conducting elements by spread out electrons after the plasma section might prompt to big of an response, while the BPMs from experience seem not to be prone to such a systematic error. The second reason is a more scientific one. In order to compare the charge before and after the interaction the measuring devices should balance to $\Delta Q = 0$ in vacuum, or show a constant offset. Figure (2.8) shows the offset between the charge measured by the BPM nearest to the interaction point upstream (USBPM) and downstream (DSBPM) of it. Each datapoint shows the mean and the standard deviation of the shot-by-shot offset of a dataset. The black line depicts the long term mean of

$$\Delta Q^{\text{offset}} = 50.4 \pm 9.0 \text{ pC} \quad (2.15)$$

with the long-term confidence-interval depicted by the red lines. Among all possible combinations of charge measuring devices the combination USBM and DSBPM showed the most stable long-term offset and variation per dataset.

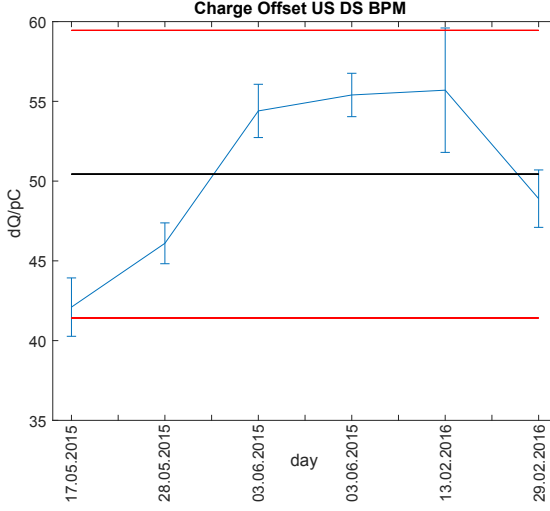


Fig. 2.8: s

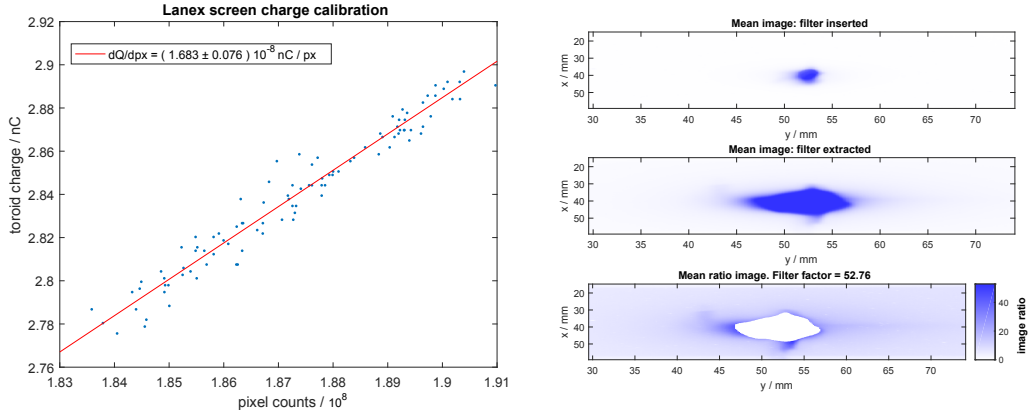


Fig. 2.9: DRZ charge calibration

Scintillating screens with a layer of phosphor - they go by by their brand name LANEX - are a successfully applied standard diagnostic for electron beams for several years now. LANEX screens are an advantageous material because of their good radiation hardness and their linear scintillation response to charge over a large range of electron energies and charge densities [53]. While in Laser-driven accelerators a LANEX screen charge calibration can be a tedious task, in PWFA experiments a well understood electron beam is conveniently available. Figure (2.9) shows the analysis of the charge calibration. The full charge 3 nC FACET electron beam was scattered at a thin foil to avoid saturation of the screen. The image, after background subtraction was cleaned of additional signal from x-rays with a morphological opening filter. The calibration images were taken with an neutral

density (ND) 2 ($T=1/100$) filter, but the witness beam data is taken without this filter to guarantee detection of all witness beams. Therefore additionally images with, and without filter inserted were taken and compared. The most intense part of the filter-in image should be compared with the mean non-saturated filter-out image which gives a total filter factor of 52.76 and a calibration of

$$Q_{\text{calib}}^{DRZ} = 88.795 \pm 4.0 \times 10^{-5} \text{ pC/px} \quad (2.16)$$

Result:

With the

2.6 *Result: Plasma Torch injection*

2.7 *Result: Trojan Horse injection*

BIBLIOGRAPHY

- [1] Francis F. Chen. *Introduction to Plasma Physics and Controlled Fusion*, volume 1. Plenum Press New York and London, 1974.
- [2] Peter Mulser and Dieter Bauer. *High power laser-matter interaction*, volume 238. Springer Science & Business Media, 2010.
- [3] MV Ammosov, NB Delone, VP Krainov, AM Perelomov, VS Popov, MV Terent'ev, Gennady L Yudin, and Misha Yu Ivanov. Tunnel ionization of complex atoms and of atomic ions in an alternating electric field. *Sov. Phys.JETP*, 64, 1986.
- [4] David L Bruhwiler, DA Dimitrov, John R Cary, Eric Esarey, Wim Leemans, and Rodolfo E Giaccone. Particle-in-cell simulations of tunneling ionization effects in plasma-based accelerators. *Physics of Plasmas (1994-present)*, 10(5):2022–2030, 2003.
- [5] R.L. Kelly. *Atomic and ionic spectrum lines below 2000A: hydrogen through argon*. Oct 1982.
- [6] Yiming Zhang, Julian RG Evans, and Shoufeng Yang. Corrected values for boiling points and enthalpies of vaporization of elements in handbooks. *Journal of Chemical & Engineering Data*, 56(2):328–337, 2011.
- [7] E. Esarey, C. B. Schroeder, and W. P. Leemans. Physics of laser-driven plasma-based electron accelerators. *Rev. Mod. Phys.*, 81:1229–1285, Aug 2009.
- [8] Pisin Chen, J. J. Su, J. M. Dawson, K. L. F. Bane, and P. B. Wilson. Energy transfer in the plasma wake-field accelerator. *Phys. Rev. Lett.*, 56:1252–1255, Mar 1986.
- [9] KL Bane, Perry B Wilson, and T Weiland. Wake fields and wake field acceleration. In *AIP Conf. Proc.*, volume 127, pages 875–928, 1984.
- [10] W. K. H. Panofsky and W. A. Wenzel. Some considerations concerning the transverse deflection of charged particles in radio-frequency fields. *Review of Scientific Instruments*, 27(11):967–967, 1956.
- [11] Helmut Wiedemann. *Particle Accelerator Physics*, volume 3. Springer-Verlag, 2007.
- [12] J. B. Rosenzweig. *Fundamentals of Beam Physics*. Oxford: Oxford University Press, 2003.
- [13] E.D Courant and H.S Snyder. Theory of the alternating-gradient synchrotron. *Annals of Physics*, 3(1):1 – 48, 1958.
- [14] Klaus Floettmann. Some basic features of the beam emittance. *Phys. Rev. ST Accel. Beams*, 6:034202, Mar 2003.

- [15] B. Hidding, G. Pretzler, J. B. Rosenzweig, T. Königstein, D. Schiller, and D. L. Bruhwiler. Ultracold electron bunch generation via plasma photocathode emission and acceleration in a beam-driven plasma blowout. *Phys. Rev. Lett.*, 108:035001, Jan 2012.
- [16] A. Martinez de la Ossa, C. Behrens, J. Grebenyuk, T. Mehrling, L. Schaper, and J. Osterhoff. High-quality electron beams from field-induced ionization injection in the strong blow-out regime of beam-driven plasma accelerators. *Nuclear Instruments and Methods in Physics Research Section A: Accelerators, Spectrometers, Detectors and Associated Equipment*, 740:231 – 235, 2014. Proceedings of the first European Advanced Accelerator Concepts Workshop 2013.
- [17] A. Pak, K. A. Marsh, S. F. Martins, W. Lu, W. B. Mori, and C. Joshi. Injection and trapping of tunnel-ionized electrons into laser-produced wakes. *Phys. Rev. Lett.*, 104:025003, Jan 2010.
- [18] Georg Wittig Henning Groth Yunfeng Xi Aihua Deng James Benjamin Rosenzweig David Leslie Bruhwiler Johnathan Smith Dino Anthony Jaroszynski Zheng-Ming Sheng Grace Gloria Manahan Guoxing Xia Steven Jamison Bernhard Hidding Alexander Knetsch, Oliver Karger. Downramp-assisted underdense photocathode electron bunch generation in plasma wakefield accelerators. *Physical Review Letters*, 2016.
- [19] S. G. Anderson, P. Musumeci, J. B. Rosenzweig, W. J. Brown, R. J. England, M. Ferrario, J. S. Jacob, M. C. Thompson, G. Travish, A. M. Tremaine, and R. Yoder. Velocity bunching of high-brightness electron beams. *Phys. Rev. ST Accel. Beams*, 8:014401, Jan 2005.
- [20] L Serafini and M Ferrario. Velocity bunching in photo-injectors. In *AIP conference proceedings*, pages 87–106. IOP INSTITUTE OF PHYSICS PUBLISHING LTD, 2001.
- [21] James Benjamime Rosenzweig, DB Cline, B Cole, H Figueroa, W Gai, R Konecny, J Norem, P Schoessow, and J Simpson. Experimental observation of plasma wake-field acceleration. *Physical review letters*, 61(1):98, 1988.
- [22] H Figueroa, W Gai, R Konecny, J Norem, A Ruggiero, P Schoessow, and J Simpson. Direct measurement of beam-induced fields in accelerating structures. *Physical review letters*, 60(21):2144, 1988.
- [23] Ian Blumenfeld, Christopher E Clayton, Franz-Josef Decker, Mark J Hogan, Chengkun Huang, Rasmus Ischebeck, Richard Iverson, Chandrashekhar Joshi, Thomas Katsouleas, Neil Kirby, et al. Energy doubling of 42 gev electrons in a metre-scale plasma wakefield accelerator. *Nature*, 445(7129):741–744, 2007.
- [24] CI Clarke, FJ Decker, RJ England, R Erikson, C Hast, MJ Hogan, SZ Li, M Litos, Y Nosochkov, J Seeman, et al. Facet: Slacs new user facility. *Energy [GeV]*, 23:20, 2012.
- [25] MJ Hogan, TO Raubenheimer, A Seryi, P Muggli, T Katsouleas, C Huang, W Lu, W An, KA Marsh, WB Mori, et al. Plasma wakefield acceleration experiments at facet. *New Journal of Physics*, 12(5):055030, 2010.
- [26] M Litos, E Adli, W An, CI Clarke, CE Clayton, Sébastien Corde, JP Delahaye, RJ England, AS Fisher, J Frederico, et al. High-efficiency acceleration of an electron beam in a plasma wakefield accelerator. *Nature*, 515(7525):92–95, 2014.

- [27] Spencer Gessner. *Demonstration of the Hollow channel Plasma Wakefield Accelerator*. PhD thesis, Stanford University, 2016.
- [28] S. Bulanov, N. Naumova, F. Pegoraro, and J. Sakai. Particle injection into the wave acceleration phase due to nonlinear wake wave breaking. *Phys. Rev. E*, 58:R5257–R5260, Nov 1998.
- [29] Hyyong Suk, Nick Barov, James Benjamin Rosenzweig, and E Esarey. Plasma electron trapping and acceleration in a plasma wake field using a density transition. *Physical review letters*, 86(6):1011, 2001.
- [30] RJ England, JB Rosenzweig, and N Barov. Plasma electron fluid motion and wave breaking near a density transition. *Physical Review E*, 66(1):016501, 2002.
- [31] J Grebenyuk, A Martinez de la Ossa, T Mehrling, and J Osterhoff. Beam-driven plasma-based acceleration of electrons with density down-ramp injection at flashforward. *Nuclear Instruments and Methods in Physics Research Section A: Accelerators, Spectrometers, Detectors and Associated Equipment*, 740:246–249, 2014.
- [32] C. G. R. Geddes, K. Nakamura, G. R. Plateau, Cs. Toth, E. Cormier-Michel, E. Esarey, C. B. Schroeder, J. R. Cary, and W. P. Leemans. Plasma-density-gradient injection of low absolute-momentum-spread electron bunches. *Phys. Rev. Lett.*, 100:215004, May 2008.
- [33] Karl Schmid, Alexander Buck, Christopher MS Sears, Julia M Mikhailova, Raphael Tautz, Daniel Herrmann, Michael Geissler, Ferenc Krausz, and Laszlo Veisz. Density-transition based electron injector for laser driven wakefield accelerators. *Physical Review Special Topics-Accelerators and Beams*, 13(9):091301, 2010.
- [34] AJ Gonsalves, Kei Nakamura, Chen Lin, Dmitriy Panasenko, Satomi Shiraishi, Thomas Sokollik, Carlo Benedetti, CB Schroeder, CGR Geddes, Jeroen Van Tilborg, et al. Tunable laser plasma accelerator based on longitudinal density tailoring. *Nature Physics*, 7(11):862–866, 2011.
- [35] Alexander Buck, Johannes Wenz, Jiancai Xu, Konstantin Khrennikov, Karl Schmid, Matthias Heigoldt, Julia M Mikhailova, M Geissler, B Shen, Ferenc Krausz, et al. Shock-front injector for high-quality laser-plasma acceleration. *Physical review letters*, 110(18):185006, 2013.
- [36] Karl Schmid, Alexander Buck, Christopher MS Sears, Julia M Mikhailova, Raphael Tautz, Daniel Herrmann, Michael Geissler, Ferenc Krausz, and Laszlo Veisz. Density-transition based electron injector for laser driven wakefield accelerators. *Physical Review Special Topics-Accelerators and Beams*, 13(9):091301, 2010.
- [37] G Wittig, O Karger, A Knetsch, Y Xi, A Deng, JB Rosenzweig, DL Bruhwiler, J Smith, GG Manahan, Z-M Sheng, et al. Optical plasma torch electron bunch generation in plasma wakefield accelerators. *Physical Review Special Topics-Accelerators and Beams*, 18(8):081304, 2015.
- [38] Georg Wittig, Oliver S Karger, Alexander Knetsch, Yunfeng Xi, Aihua Deng, James B Rosenzweig, David L Bruhwiler, Jonathan Smith, Zheng-Ming Sheng, Dino A Jaroszynski, et al. Electron beam manipulation, injection and acceleration in plasma wakefield accelerators by optically generated plasma density spikes. *Nuclear Instruments and Methods in Physics Research Section A: Accelerators, Spectrometers, Detectors and Associated Equipment*, 2016.

- [39] N. Vafaei-Najafabadi, K. A. Marsh, C. E. Clayton, W. An, W. B. Mori, C. Joshi, W. Lu, E. Adli, S. Corde, M. Litos, S. Li, S. Gessner, J. Frederico, A. S. Fisher, Z. Wu, D. Walz, R. J. England, J. P. Delahaye, C. I. Clarke, M. J. Hogan, and P. Muggli. Beam loading by distributed injection of electrons in a plasma wakefield accelerator. *Phys. Rev. Lett.*, 112:025001, Jan 2014.
- [40] A. Pak, K. A. Marsh, S. F. Martins, W. Lu, W. B. Mori, and C. Joshi. Injection and trapping of tunnel-ionized electrons into laser-produced wakes. *Phys. Rev. Lett.*, 104:025003, Jan 2010.
- [41] A. Martinez de la Ossa, J. Grebenyuk, T. Mehrling, L. Schaper, and J. Osterhoff. High-quality electron beams from beam-driven plasma accelerators by wakefield-induced ionization injection. *Phys. Rev. Lett.*, 111:245003, Dec 2013.
- [42] Y Xi, B Hidding, D Bruhwiler, G Pretzler, and JB Rosenzweig. Hybrid modeling of relativistic underdense plasma photocathode injectors. *Physical Review Special Topics-Accelerators and Beams*, 16(3):031303, 2013.
- [43] B Hidding, GG Manahan, O Karger, A Knetsch, G Wittig, DA Jaroszynski, ZM Sheng, Y Xi, A Deng, JB Rosenzweig, et al. Ultrahigh brightness bunches from hybrid plasma accelerators as drivers of 5th generation light sources. *Journal of Physics B: Atomic, Molecular and Optical Physics*, 47(23):234010, 2014.
- [44] K Kim, I Alexeev, and H Milchberg. Single-shot measurement of laser-induced double step ionization of helium. *Optics express*, 10(26):1563–1572, 2002.
- [45] G. G. Manahan, A. Deng, O. Karger, Y. Xi, A. Knetsch, M. Litos, G. Wittig, T. Heinemann, J. Smith, Z. M. Sheng, D. A. Jaroszynski, G. Andonian, D. L. Bruhwiler, J. B. Rosenzweig, and B. Hidding. Hot spots and dark current in advanced plasma wakefield accelerators. *Phys. Rev. Accel. Beams*, 19:011303, Jan 2016.
- [46] S Z Green, E Adli, C I Clarke, S Corde, S A Edstrom, A S Fisher, J Frederico, J C Frisch, S Gessner, S Gilevich, P Hering, M J Hogan, R K Jobe, M Litos, J E May, D R Walz, V Yakimenko, C E Clayton, C Joshi, K A Marsh, N Vafaei-Najafabadi, and P Muggli. Laser ionized preformed plasma at facet. *Plasma Physics and Controlled Fusion*, 56(8):084011, 2014.
- [47] Allied Vision, <https://www.alliedvision.com/en/products/cameras/detail/Manta/G-125.html>. *Manta G-125 Data sheet*.
- [48] Klaus R Mann, G Pfeifer, and Guenter Reisse. Damage threshold measurements using femtosecond excimer laser. In *Optical Materials for High Power Lasers*, pages 415–423. International Society for Optics and Photonics, 1993.
- [49] CB Li, TQ Jia, HY Sun, XX Li, SZ Xu, DH Feng, XF Wang, XC Ge, and ZZ Xu. Theoretical and experimental study on femtosecond laser-induced damage in mgf₂ crystals. In *ICO20: Lasers and Laser Technologies*, pages 60281L–60281L. International Society for Optics and Photonics, 2006.
- [50] Robert Adair, L. L. Chase, and Stephen A. Payne. Nonlinear refractive index of optical crystals. *Phys. Rev. B*, 39:3337–3350, Feb 1989.

- [51] X. Yan, A. M. MacLeod, W. A. Gillespie, G. M. H. Knippels, D. Oepts, A. F. G. van der Meer, and W. Seidel. Subpicosecond electro-optic measurement of relativistic electron pulses. *Phys. Rev. Lett.*, 85:3404–3407, Oct 2000.
- [52] Bernd Richard Steffen. *Electro-Optic Methods for Longitudinal Bunch Diagnostics at FLASH*. PhD thesis, University of Hamburg, 2007.
- [53] Alexander Buck, K Zeil, Antonia Popp, Karl Schmid, A Jochmann, SD Kraft, B Hidding, T Kudyakov, CMS Sears, Laszlo Veisz, et al. Absolute charge calibration of scintillating screens for relativistic electron detection. *Review of Scientific Instruments*, 81(3):033301, 2010.